Mon. Not. R. Astron. Soc. **000**, 1–?? (2018) Printed 7 April 2020 (MN LATEX style file v2.2)

Properties of the Lenses in the South Pole Telescope survey.

K. M. Rotermund[1⋆], S. C. Chapman[1], J. D. Vieira[2], etc.

[1] *Department of Physics and Atmospheric Science, Dalhousie University, Halifax, NS, B3H 4R2, Canada*
[2] *Department of Astronomy and Department of Physics, University of Illinois, 1002 West Green Street, Urbana, IL 61801, USA*

In Prep for publication in MNRAS

ABSTRACT

We present the properties of the 100 gravitational lens galaxies uncovered in the South Pole Telescope (SPT) survey of dusty, thermal spectrum sources over 2500 deg^2. We present optical and near-infrared imaging identifying the lenses, and spectroscopic redshifts complete for 50% of the sample. We compare the properties of the lenses to lenses discovered through other surveys (SLACS, BELLS, Herschel), and highlight differences from our source selected sample. Our lens sample clearly extends to higher redshifts and shows a larger diversity in lens luminosities, colors (SEDs) and morphologies than optical *lens-selected* samples. We discuss implications for lensing cross sections and future lensing surveys.

Key words: galaxies: abundances – galaxies: high-redshift – gravitational lensing.

1 INTRODUCTION

The serendipitous alignment of a massive foreground galaxy and a high-redshift galaxy results in strong gravitational lensing in which light from the background galaxy is both distorted and amplified as it is bent around the foreground galaxy in a manner that is unique to that lensing system. This process confirms Einstein's theory of General Relativity and is an incredibly powerful tool in determining key properties of both the massive foreground galaxy, the lens, as well as the high-redshift dusty, star-forming galaxy (DSFG), the source.

Strong gravitational lensing is not a frequent occurrence and requires expensive large-field surveys for initial detections. Early surveys, such as the Cosmic Lens All-Sky Survey (CLASS; Myers et al. 1998) and the Jodrell Bank Very Large Array gravitational lens survey (JVAS; King & Browne 1996), were conducted using radio frequencies and resulted in a sample of $\sim$ 80 strong lenses. More recently, optical follow-up surveys were conducted for candidates initially selected from the Sloan Digital Sky Survey (SDSS) using the Sloan Lens Advanced Camera for Surveys (SLACS; Bolton et al. 2006, 2008) and the SDSS-III Baryon Oscillation Spectroscopy Survey (BOSS; Eisenstein et al. 2011), specifically the BOSS Emission-Line Lens Survey (BELLS; Brownstein et al. 2011), more than doubling confirmed lenses.

However, the dusty, star-forming galaxy's UV-radiation is predominantly absorbed by the abundant intra-galactic gas and dust and is re-emitted in the far-infrared (FIR) and (sub)millimeter wavelengths. Wide-field surveys conducted in the (sub)mm such as by the South Pole Telescope (SPT; Carlstrom et al. 2011; Vieira et al. 2010) and by the *Herschel Space Observatory* (*Herschel*, Pilbratt et al. 2010, Bussmann et al. 2013) are therefore more comprehensive and unbiased in their selection of sources compared to the previous radio surveys.

Beginning in 2007, the SPT conducted a $2,500$ deg^2 survey in the millimeter regime. Point sources were identified - those with dust-like spectral indexes ($S_{1.4\mathrm{mm}}/S_{2.0\mathrm{mm}} > 2$) were selected while rejecting synchrotron sources, low-redshift objects, and those found in the IRAS Faint Source Catalog. The initial $1,300$ deg^2 survey resulted in a compilation of 47 sources with $S_{1.4\mathrm{mm}} > 20$ mJy (Vieira et al. 2010). More details regarding SPT's selection criteria can be found in Weiß et al. (2013) with further information regarding de-boosting of flux densities in Vieira et al. (2010) and Crawford et al. (2010). Initial follow-up observations were conducted with LABOCA at 870 μm. The higher spatial resolution of LABOCA refined the source locations. 26 SPT sources were observed with ALMA Cycle 0 in the 3 mm band, resulting in spectroscopic redshifts for 24 sources (Weiß et al. 2013). Through a combination of ALMA Cycle 1 in the 3 mm band and APEX/FLASH and APEX/SEPIA observations, spectroscopic redshifts for an additional 15 SPT sources were determine (Strandet et al. 2013). Follow-up imaging with ALMA identified image morphologies unique to gravitational lensing for the majority of the greater sample (Vieira et al. 2013), leading to substantial efforts in creating lens models for each of the gravitational lensing systems (Hezaveh et al. 2013, Spilker et al. 2016). Including the full $2,500$ deg^2 survey brings the SPT DSFG sample size to $\sim$ 100, the majority of which are gravitationally lensed.

The flux limited, millimeter wavelength, $2,500$ deg^2 SPT survey has the distinct advantage of selecting submillimeter galaxies (SMG) independent of their redshift due to the effects of negative K-correction, in which the SMG's rising dust spectrum compensates for any cosmological dimming (Vieira et al. 2013). In this

⋆ kaja@dal.ca

© 2018 RAS

work we will present data and detailed analysis for the lenses of $\sim$ 100 gravitational lensing systems discovered by the SPT survey. Follow-up optical and near-IR photometry and spectroscopy was commissioned from the Very Large Telescope (VLT) and GEMINI-South, and previously published ancillary photometric data was obtained from the *Hubble Space Telescope* (*Hubble*), the *Spitzer Space Telescope* (*Spitzer*), and the Atacama Large Millimeter/submillimeter Array (ALMA).

This paper is organized as follows. In Section 2 we outline the optical and near-IR photometry and spectroscopy measurements taken. Section 3 discusses lens environments. Our results, including redshifts, color, Einstein radii, and masses are presented in Section 4. Throughout this work, we assume a flat ΛCDM cosmology, $h = 0.71$, $\Omega_m = 0.27$, $\Omega_\Lambda = 0.73$.

2 OBSERVATIONS

We initiated a campaign to obtain multi-band photometry of the SPT lenses throughout the optical, near-IR and mid-IR. Table 1 summarizes the multi-band data presented in this paper while Table 2 provides more details on observing hours. We commissioned optical imaging in the $g-$ and $R-$bands from VLT's FORS2 as well as GEMINI-South's GMOS camera. We received near-IR F110W, F140W, and F160W imaging from *HST*'s WFC3 and J_s- and K_s-band imaging from VLT's ISAAC, GEMINI-S's FLAMINGOS2 as well as Magellan's MMIRS cameras. Lastly, we also obtained mid-IR imaging from *Spitzer*'s IRAC Channels 1 and 2. Spectroscopy was also commissioned from VLT-FORS2 and GEMINI-S GMOS in order to determine robust redshifts.

2.1 Optical and Near-IR Imaging

Deep imaging in the optical ($g-$ and $R-$ band) and near-IR ($J-$ and K_s- band) were taken with VLT's FORS2 and ISAAC cameras respectively at the European Southern Observatory (ESO) in Paranal, Chile, as well as with Gemini-South's GMOS-S and FLAMINGOS-2 cameras, also respectively, in Cerro Pachon, Chile. Standard observing strategies were adhered to as observations were being made in service mode under photometric conditions. A basic reduction process was applied to the data. Thermal sky images over 15 min intervals were created and then subtracted from the raw data. The sky-subtracted images were then combined into mosaics, which were calibrated to the astrometry and photometry of 2MASS and USNO catalogs. The seeing, as derived from the FWHM size of stars in each frame, ranges from $0.6''$ to $0.8''$. The 5σ Vega magnitude depths achieved are $K_s = 21.5$, $R = 25.8$, and $g = 26.1$.

50 of the SPT DSFGs were followed up using IRAC on *Spitzer* at 3.6 and 4.5 μm. The data processing procedure can be found in Ma et al. (2015). The final mosaics have a resampled pixel scale of $0.6''$pixel^{-1} and an angular resolution of $\sim 1.7''$.

Observations for a subsample of 18 SPT DSFGs were done using *HST*'s WFC3 bands F110W and F160W, while F140W was used for an additional six, as presented in Ma et al. (2015). *HST*standard reduction pipelines were implemented and resulted in a pixel scale of $0.128''$.

2.2 Spectroscopy

Optical spectroscopy was performed for $\sim$ 70 % of the lenses. Primarily ESO's VLT was used, either with the X-SHOOTER medium resolution spectrograph (Vernet et al. 2011) mounted on the UT2 Cassegrain focus (Kueyen) or with FORS2 (Appenzeller et al. 1998), a varying-resolution spectrograph mounted on the UT1 Cassegrain focus. GEMINI's GMOS-S (Hook et al. 2004, Allington-Smith et al. 2002) is another spectrograph from which observations were commissioned. Table 2 provides a list of program ID's and their respective hours of observation.

Table 1. Optical and Near-IR Imaging

Telescope-Instrument	Filter ID	λ [μm]	AB-Vega
VLT - FORS2	g	0.47	-0.08
(Gemini - GMOS)	R	0 .64	0.21
HST- WFC3	F110W	1.150	0.76[1.62*]
	F140W	1.4	1.08[2.03*]
	F160W	1.545	1.25[2.24*]
VLT - ISAAC	Js	1.24	0.91
(Magellan - MMIRS)	Ks	2.16	1.85
Spitzer- IRAC	1	3.550	2.79
	2	4.493	3.26

Note: * *HST*'s zero point of 21.10 is for the ST magnitude system: STmag-ABmag

Table 2. Commissioned Programs

Telescope	PID	Instrument	Time
VLT	092.A-0480(A)	XSHOOTER	32hrs
	090.A-0503(A)	FORS2	8hrs
	090.A-0503(B)	FORS2	33hrs
	090.A-0503(C)	ISAAC	1.4ni
	088.A-0902(A)	ISAAC	16hrs
	088.A-0902(B)	ISAAC	16hrs
	088.A-0902(C)	FORS2	4hrs
	088.A-0902(D)	FORS2	24hrs
	086.A-0797(A)	ISAAC	4.0ni
	285.A-5034(A)	FORS2	0.5hrs
	285.A-5034(B)	FORS2	2.0hrs
	085.A-0608(A)	ISAAC	3.0ni
	284.A-5029(A)	ISAAC	4hrs
	284.A-5029(B)	XSHOOTER	2hrs
	284.A-5029(C)	ISAAC	2hrs
	284.A-5029(D)	XSHOOTER	4hrs
Gemini	GS-2013B-Q-5	GMOS	20hrs
	GS-2013A-Q-33	GMOS	20hrs
	GS-2016B-Q-68	GMOS & FLAMINGOS-2	33hrs

2.2.1 *X-SHOOTER*

Predominantly the X-SHOOTER echelle spectrograph was used, with which near-continuous spectra from 0.3 μm to 2.48 μm were obtained by stitching together three wavelength regimes: ultraviolet (UV), optical (OPT), and near-infrared (NIR). The slit length is fixed across all bands at $11''$, while the slit width can be varied. For our measurements the slit widths were set to $1.0''$(UV), $0.9''$(VIS), and $0.9''$(NIR). The resolving powers attained were

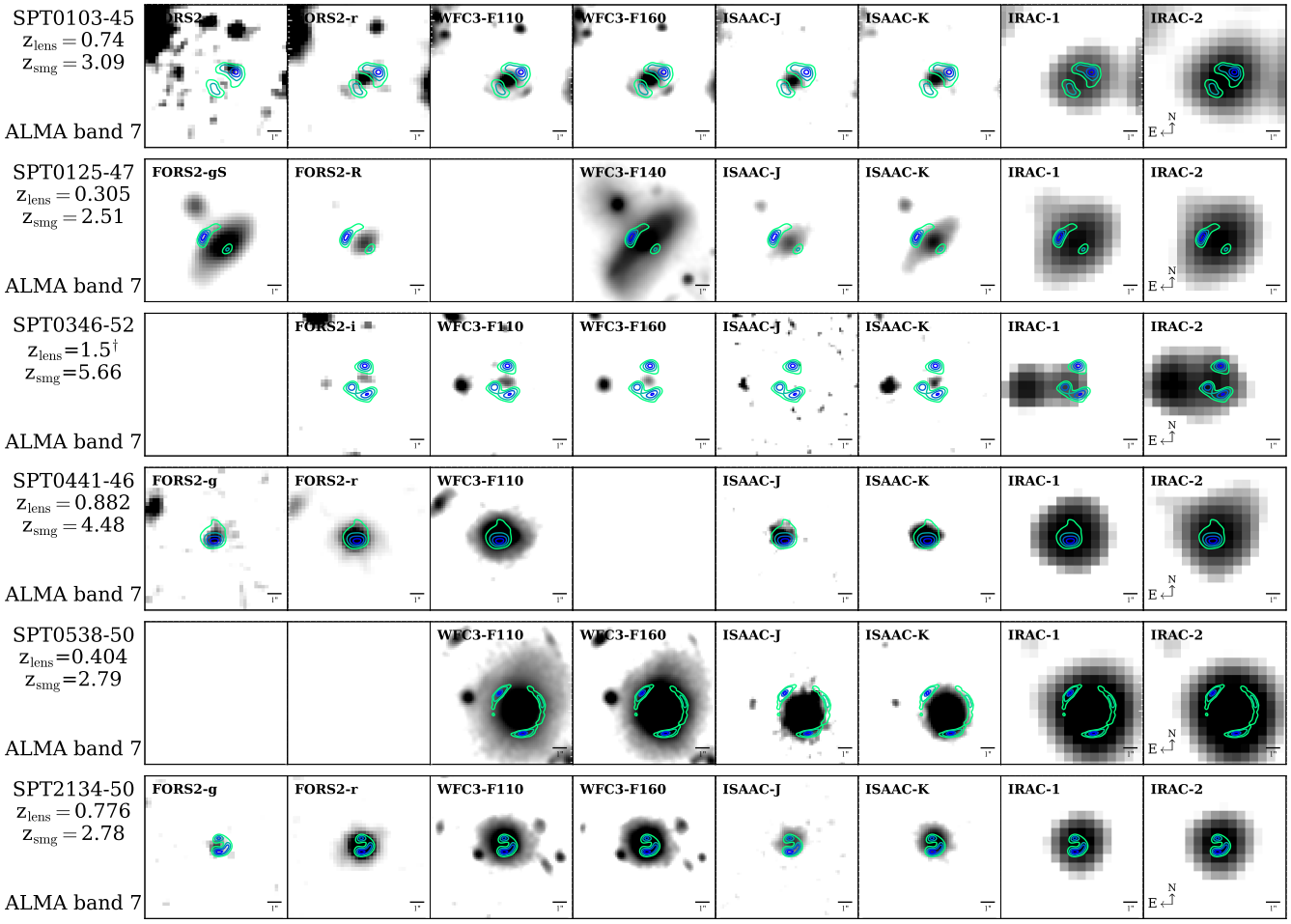

$R = 5100$ (UV), 6700 (OPT), and 5000 (NIR). Six integrations of 1300 sec (UV), 1355 sec (OPT), and 480 sec (NIR) exposures were completed for a total of 2:10 hrs, 2:15:30 hrs, and 48 min on-source time respectively. Observations were done over a 10 month period ranging from October 29, 2013 to July 1, 2014. The airmass ranged approximately from 1.1 to 1.4 and the airmass corrected seeing varied from 0.9 to 1.2.

The standard ESO pipeline (Modigliani et al. 2010) was used for data preparation and reduction. Briefly, pixels with non-linear responses are flagged in a non-linear bad pixel map. A standard kappa sigma clipping technique is used to remove count outliers in the median stack-combined bias frame. Similarly dark frames are median stack-combined to create a master dark frame in which noisy pixels and cosmic rays are flagged and removed. In the slit nod mode raw frames in dither positions A and B are initially co-added separately before they are subtracted from each other such that, to first order, the sky is removed, before being combined into a single frame. The three different wavelength echelle orders are subsequently combined to create a continuous spectrum. Finally the 2D product can be collapsed on designated slit positions to create 1D spectra.

2.2.2 *FORS2*

FORS2 spectroscopy was obtained for x? additional lenses. Lenses were first target with pre-imaging in $R-$band (and occasionally in $g-$band) before spectral scans were acquired. Multi-object spectroscopy (MXU) masks were used in service mode. The slit width and slit length varied with each lens. SPT2031-51 slit width and length were set to 1.0″and 4.0″. The lenses were observed with the GRIS_300V grism and GG435 filter. This combination results in a wavelength range from 445 nm to 865 nm and a dispersion of 112 Å/mm. Integration times also varied with lens. Typically three integrations were taken with 500 sec to 900 sec exposure times, leading to a range of total on-target time from 25 min to 45 min. Data was collected over x months from xx to yy, over which the seeing predominantly remained $< 1.0''$and the airmass ranged from 1.5 to 1.8.

The standard FORS2 spectroscopic pipeline (Izzo et al. 2017) was used for data reduction. First a master bias frame is created from the raw bias exposures. Next flat and arc calibration lamp exposures are used to create a spectral extraction mask as well as a normalized flat field frame which are then applied to the science exposures.

2.2.3 *GMOS-S*

2.3 Ancilliary Data

The ALMA interferometer, located in the Atacama desert on the Chajnantor Plateau in northern Chile, was used to observe the SPT SMGs with incredibly high resolution. Predominantly, the SMGs were observed at 870 μm during Cycle 0 program 2011.0.00958.S

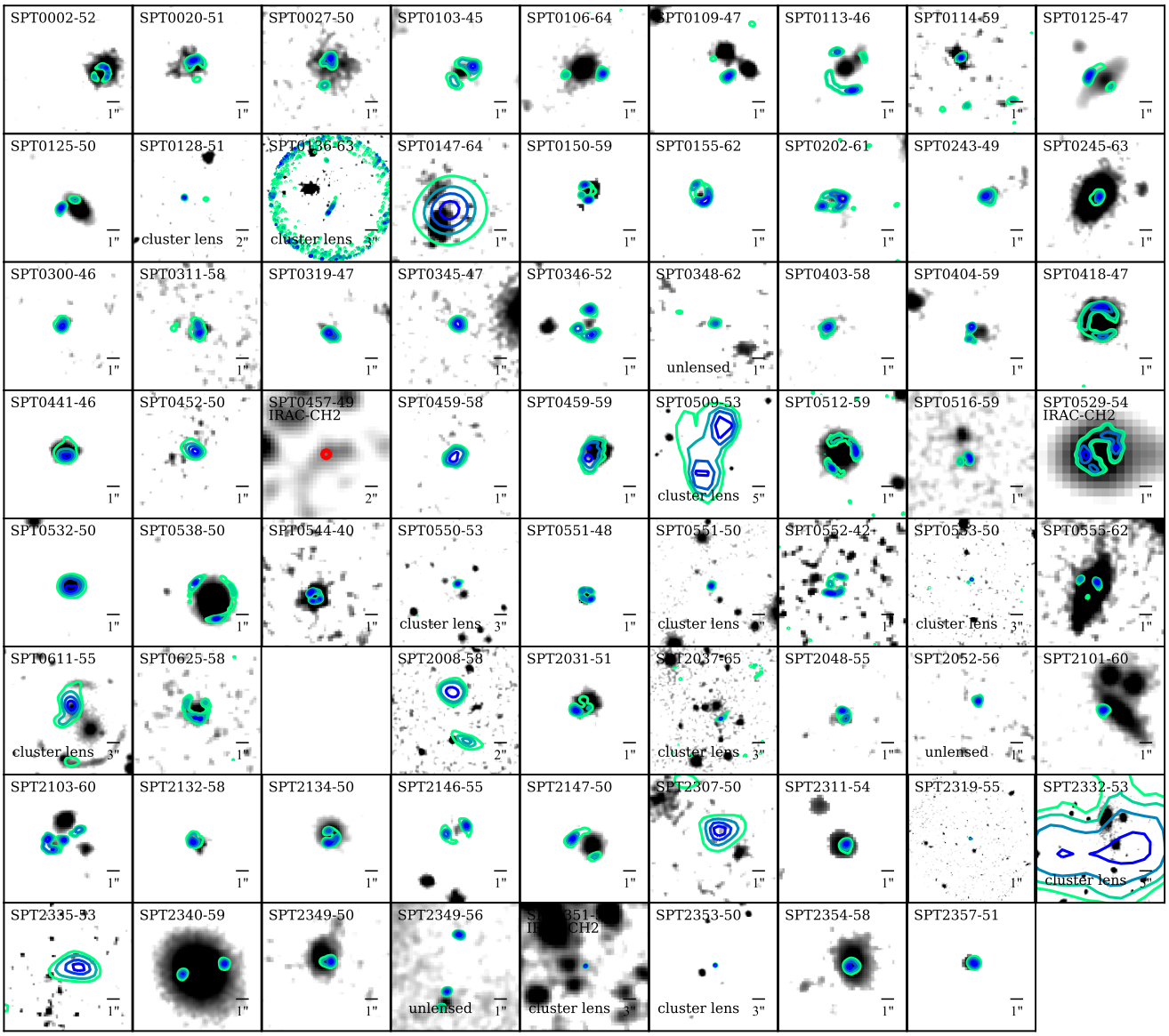

(PI D. Marrone) with additional observations made at 3 mm in later cycles (Cycles 2 and 3). Details of the imaging can be found in Spilker et al. (2016), while a concise description of the source redshift determination can be found in Weiß et al. (2013) and Strandet et al. (2016).

3 LENS CLASSIFICATIONS

ALMA imaging showed that a majority of sources resolved into a primary image with one or more counter-images. The vast majority of the submm galaxies identified by the SPT survey belong to a lensing system in which the lens is a single massive galaxy. If imaging does not display the tell-tale sign of Einstein rings, it is likely that the lens is either a group/cluster lens, is not very massive, or the lensing system is poorly aligned. If none of these scenarios can be verified, it is possible that the source is an unlensed candidate. The lens type can be initially identified through a visual inspection of the imaging and then confirmed via lens models.

3.1 Galaxy-Galaxy Lensing

The most common form of strong gravitational lensing in the SPT sample occurs via a single massive galaxy in the foreground, referred to as "galaxy-galaxy" lensing. Our sample consists of 56 such lensing systems. The lenses are expected to be massive, low-redshift galaxies, predominantly ellipticals. Ellipticals contain minimal interstellar gas and dust, thus evolve passively, presenting little to no active star formation. They are host to an old stellar population suggesting that they should be visible in the optical and near-IR. From a visual inspection of the image morphologies, the majority of the single galaxy lenses are indeed massive ellipticals. A small fraction, < 15 %, display morphologies indicative of active star-formation such as spiral galaxies, tidal tails, companion galaxies, *etc.*, and will be explored in Sect. 4.2.

3.2 Cluster & Group Lenses

In roughly a dozen cases, the high-z SMG is lensed by more than one foreground object. The lens can consist of just a couple of

galaxies, in which case the counter-images of the source may have similar morphologies as galaxy-galaxy lensing or configure in more unique shapes. Lens modeling conducted by Spilker et al. (2016) found five of the original 47 SMGs to be lensed by a system of 2-3 galaxies (SPT0020-51, SPT0027-50, SPT0109-47, SPT0113-46, and SPT2103-60). These are confirmed group lenses. Photometric values were extracted for the center-most galaxy of the lens.

The lens can also be a galaxy cluster. In such instances it is rare to find more than one source image due to the broad and diffuse mass distribution of the lens. We have identified nine additional candidate group or cluster lenses (SPT0128-51, SPT0136-63, SPT0550-53, SPT0551-50, SPT0553-50, SPT0611-55, SPT2037-65, SPT2351-57, and SPT2353-50). A photometric analysis was not done for these lenses.

3.3 Unlensed Candidates

If the image morphology of the SMG does not exhibit any features of gravitational lensing, and, importantly, no foreground lens is observed in the optical or near-IR, then the SMG is a candidate unlensed galaxy. The subset of unlensed SMGs is small and contains some of the most intrinsically luminous galaxies of the sample. To date, the SPT-SMG sample consists of three confirmed unlensed galaxies (SPT0348-62, SPT2052-56, and SPT2349-56) with six additional unlensed candidates. A detailed and ongoing analysis of the confirmed unlensed SMGs has been conducted by Miller et al. (2018) and others.

4 RESULTS

4.1 Redshift Distribution

Determining robust redshifts for the SPT lenses is challenging. Spectra for the sub-sample of lenses from which redshifts were determined are shown in Appendix **??**. The lack of intra-galactic gas and dust in ellipticals results in sparse and weak emission lines. Furthermore many lenses are too faint to attempt spectroscopic observations. As an alternative, we have used the $K-z$ relation, an empirical relation initially observed for radio ellipticals, to approximate single-band photometric redshifts. We use the sub-sample for which spectroscopic redshifts are known to determine the $K-z$ relation, $K = 3.24z + 16.64$. Figure 1 plots the $K-$band magnitude as a function of redshift. Spectroscopic redshifts (of which there are 25) are shown as solid diamonds while photometric $K-z$ redshifts are shown as open diamonds. (Stars are used to identify lenses with strong [O II] detections.)

We compare the redshift distribution of the SPT sample with other surveys of gravitational lenses. The *Herschel* sub-sample (Bussmann et al. 2013) is a source-selected sample similar to our own SPT survey, in which gravitational lensing systems are identified first by their high-z SMG source. The SLACS (Auger et al. 2009) and BELLS (Brownstein et al. 2011) samples were selected spectroscopically from the magnitude-limited SDSS database and are lens-selected surveys. Fig. 2 shows the spectroscopic redshift distribution for the SPT lenses in shaded red in comparison to the SLACS sample in purple, the BELLS sample in grey, and the *Herschel* sub-sample in green. The SLACS and BELLS surveys have narrow, low-redshift distributions, a consequence of their selection criteria. The source-selected *Herschel* sub-sample spans a redshift range nearly identical to that of SPT. The $K-z$ photometric redshifts for the SPT lenses are shown in blue. They suggest that the median redshift of gravitational lenses is higher than the spectroscopic data from either the lens- or source-selected samples would imply.

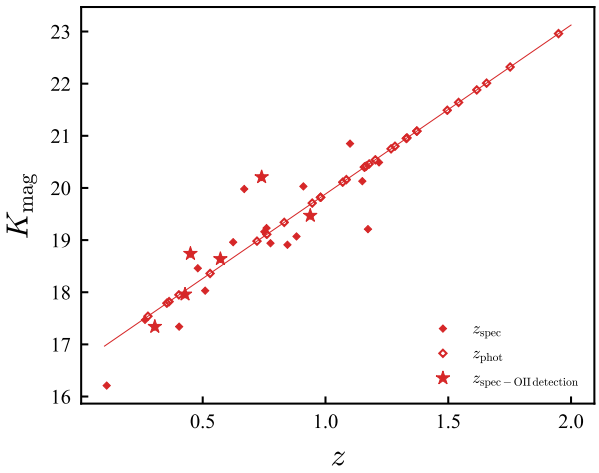

Figure 1. $K-$band magnitude as a function of redshift. A linear regression (solid red line) is applied to lenses with spectroscopic redshift (solid diamonds). $K-z$ redshifts (open diamonds) are calculated for lenses without spectroscopic redshifts. Lenses with significant [O II] detections are identified by star symbols.

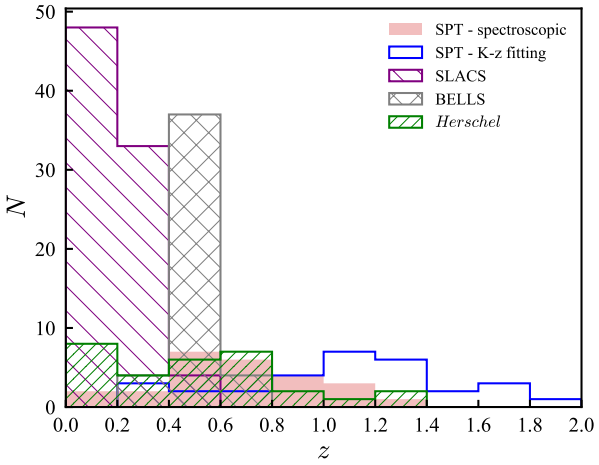

Figure 2. Lens redshift distribution. Spectroscopic redshifts for the SPT sample are in shaded red while the $K-z$ fitting redshifts are outlined in blue.

4.2 Star formation in galaxy-galaxy lenses

In addition to a visual inspection of the imaging to identify lens type we also considered the color of the lens and the equivalent width of the [O II] emission feature, when available. We compare the $J-K$ and the $R-K$ color for the lenses to that of a typical 5 Gyr. elliptical galaxy determined using the SWIRE template (Polletta et al. 2007), black curve in Fig. 3. We find that ~ 75 % (~ 80 %) of all lenses lie within 0.5 (1) magnitude of the $J-K$ ($R-K$) template color.

A strong Hα recombination line is commonly used to indicate high SFRs. Unfortunately the Hα line at $6,562.8$ Å is

frequently inaccessible to current spectrographs for galaxies past $z > 0.5$ as the near-IR contains many strong sky lines. Ly et al. (2012) demonstrated that for a population of $z \sim 1.5$ galaxies, the luminosity of the singly-ionized oxygen [O II] emission feature is strongly correlated with the UV continuum, $\log L([\mathrm{O\ II}]) \propto (0.89 \pm 0.22) \times \log L(1,500/\text{Å})$. An older stellar population is not energetic enough to ionize neutral hydrogen, let alone heavier elements such as oxygen. In contrast, emission from the hot, short-lived O and B type stellar population are a driving force behind the ionization of the interstellar medium. Therefore the strength of the [O II] doublet ($\lambda_{\rm rest} = 3,727\ \&\ 3,729$ Å) can be used as a SFR indicator instead of Hα.

1D spectra containing the [O II] doublet were extracted for 17 lenses, they can be found in Appendix **??**. The left column shows the full spectrum extracted for each lens and the right column is centered on the rest wavelength of the [O II] line. A gaussian fit to the [O II] peak was attempted for all lenses. Four lenses (SPT0103-45, SPT0125-47, SPT0459-59, and SPT2349-50) exhibited robust [O II] detections ($> 3\times$RMS), three having an equivalent width greater than 1. Lenses with [O II] detections are labelled as "star forming" in Fig. 4. If [O II] was not detected an upper limit on the equivalent width was determined from the RMS and channel width of the spectrum.

We find that only ~ 12 % of the lenses in the SPT-SMG sample display strong evidence of active star formation (*i.e.* clear confirmation of a disc-like spiral structure in the morphology or from both the color and an [O II] line detection). The vast majority, the remaining ~ 88 %, are therefore passively evolving ellipticals or show inconclusive evidence of star formation.

4.3 1.6 μm Luminosity

For a more detailed comparison of the lenses, we consider the 1.6 μm luminosity. SLACS, BELLS, and *Herschel* measured observed $i-$band magnitudes. We convert these into rest-frame 1.6 μm luminosities by applying an $i-$band scaling ratio determined from the SED template of a typical 5 Gyr. elliptical galaxy Polletta et al. (2007) redshifted to that lens' redshift and our adopted rest-frame, the median redshift of the SLACS sample ($z \sim 0.204$). For our own SPT lenses, we apply a similar technique, however $J-$ and $K-$bands are more appropriate observing bands for higher redshift lenses and are used instead. In the top panel of Fig. 5 the observed $i-$band luminosities are plotted as a function of redshift (left y-axis). A mass-to-light ratio determined from the SLACS sample and adopted for the remaining samples allows us to approximate a 1.6 μm stellar mass for the lenses (right y-axis). The dashed (dash-dotted) [dotted] black line is the $i-$band ($J-$band) [$K-$band] luminosity determined from the 5 Gyr. elliptical galaxy SED template created by Polletta et al. (2007) as it is redshifted. The bottom plot in Fig. 5 plots the rest-frame 1.6 μm luminosities as a function of redshift. Solid lines and the surrounding shaded regions are the running average and RMS for the relevant sample. For the SLACS and BELLS samples the luminosity is a sharply rising function of redshift, even over their short redshift ranges, a consequence of their selection criteria. In order for higher-z lenses to be selected they must be intrinsically more luminous (more massive) than the lower-z lenses. As our SPT lenses do not suffer this selection effect, we are able to probe the true mass range of lenses, finding a significant fraction of lower mass lenses in our sample. We note that we do not identify any lenses as massive as the upper 30 % of the SLACS and BELLS lenses. This could be a result of our high source redshift bias ($z > 2$) from the SPT 1.4 mm selection effect.

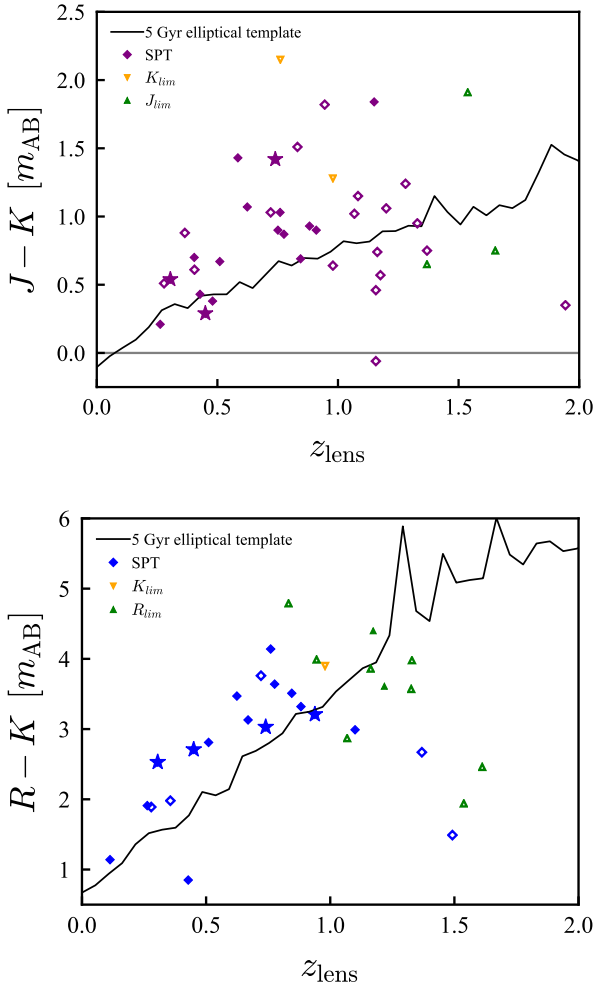

Figure 3. Color-magnitude diagrams. Difference in $J-$ and $K-$band magnitude (*left*) and difference in $R-$ and $K-$band magnitude (*right*) as a function of redshift. Lenses which have spectroscopic redshifts are shown as solid symbols, lenses with photometric redshifts are shown as open symbols. Triangles indicate when the lens was not detected in a given band and a limit was used. Stars indicate lenses with significant [O II] detections. The solid black line represents the color for the SED template of a typical 5 Gyr. elliptical galaxy created by Polletta et al. (2007)

4.4 Modeling the Redshift Distibution

5 CONCLUSION

ACKNOWLEDGMENTS

Based on observations obtained at the Gemini Observatory, which is operated by the Association of Universities for Research in Astronomy, Inc., under a cooperative agreement with the NSF on behalf of the Gemini partnership: the National Science Foundation (United States), the National Research Council (Canada), CONICYT (Chile), the Australian Research Council (Australia), Ministério da Ciência, Tecnologia e Inovação (Brazil) and Ministerio de Ciencia, Tecnología e Innovación Productiva (Argentina). a collaboration between the Max-Planck-Institut fur Radioastronomie,

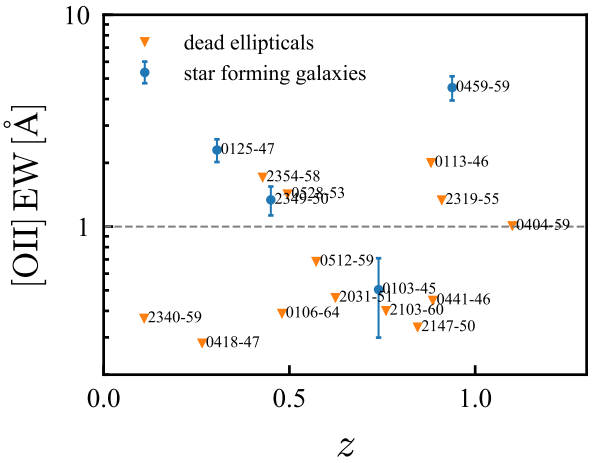

Figure 4. [O II] equivalent width determined from 1D spectra. [O II] detections above 3×RMS are categorized as "star forming galaxies." Galaxies with no discernible [O II] feature are labelled "dead ellipticals." An upper limit on the equivalent width is determined from the RMS and channel width of the spectrum.

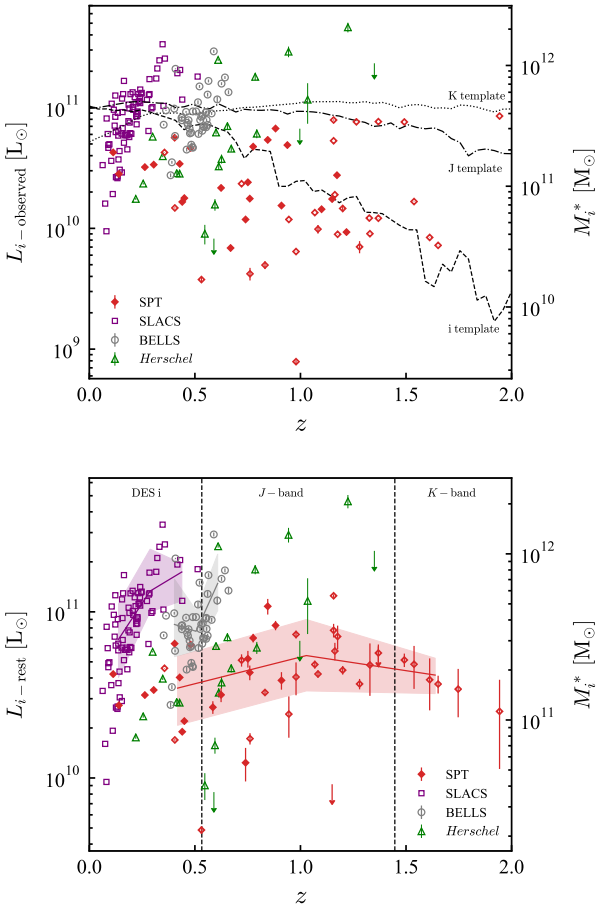

Figure 5. *Top:* Observed $i-$band luminosity as a function of redshift. The dashed (dash-dotted) [dotted] black line is the $i-$band ($J-$band) [$K-$band] luminosity determined from the 5 Gyr. elliptical galaxy SED template created by Polletta et al. (2007) as it is redshifted. *Bottom:* Rest-frame 1.6 μm luminosity as a function of redshift. Solid lines and the surrounding shaded regions are the running average and RMS for the relevant sample.

the European Southern Observatory, and the Onsala Space Observatory. This paper makes use of the following ALMA data: ADS/JAO.ALMA#2011.0.00957.S. ALMA is a partnership of ESO (representing its member states), NSF (USA) and NINS (Japan), together with NRC (Canada) and NSC and ASIAA (Taiwan), in cooperation with the Republic of Chile. The Joint ALMA Observatory is operated by ESO, AUI/NRAO and NAOJ. Based on observations taken with European Southern Observatory Very Large Telescope, Paranal, Chile, with programme ID 088.A-0902(C), 090.A-0503(A) and 092.A-0480(A), and with the Atacama Pathfinder Experiment under programme ID 086.A-0793(A) and 087.A-0815(A). SCC acknowledges support from NSERC and CFI, the Aspen Center for Physics where this manuscript was discussed.

REFERENCES

Bothwell M., et al., 2013, MNRAS, 205, 1511
Chiang et al. 2013 ApJ, 779, 127
Cooper M., et al. 2008, MNRAS, 390, 245
Daddi E., et al., 2008, ApJ, 673, L21
Decarli, R.,et al. 2014, ApJ, 782, 78
Elbaz D., et al., 2007 A&A, 468,33
Elbaz D., et al., 2011 A&A, 533,119
Erb D., et al., 2011, ApJ, 740L, 31
Franx M., et al., 2003, 587L, 79
Hainline L., et al. 2011, ApJ, 740, 96
Harris, A. I., et al. 2012, ApJ, 752, 152
Hilton, M., et al. 2010, ApJ, 718, 133
Hopkins, P., et al., 2008, ApJS, 175, 390
Ivison R., et al., 2011, MNRAS, 412, 1913
Jorgensen, I., et al., 2006, ApJ, 639L, 9
Kauffmann et al., 1993, MNRAS, 264, 201
King, L. J., & Browne, I. W. A. 1996, MNRAS, 282, 67
Ma, C. J., et al. 2015, ApJ, submitted
Myers, S. T., et al. 2003, MNRAS, 341, 1
Peter et al. 2007, ApJ, 668, 23
Rettura et al., 2010, ApJ, 709, 512
Riechers D., et al., 2010 ApJ, 724,153
Smail, I., et al. 2014, ApJ, 782, 19
Steidel, C., et al 2011, ApJ, 736, 60
Steidel, C., et al 2005, ApJ, 626, 44
Swinbank, M., et al. 2014, MNRAS, 438, 1267
Tacconi L. J. et al., 2013, ApJ, 768, 74
Tadaki, K., et al., 2014, ApJ, 788, L23
Tran K.-V., et al., 2010, ApJ, 719L,126
van Dokkum, P., et al., 1998, ApJ, 504L, 17
Vieira, J. D., et al., 2013, Nat, 495, 344-347
Weiß, A., De Breuck, C., Marrone, D. P., et al. 2013, ApJ, 767, 88

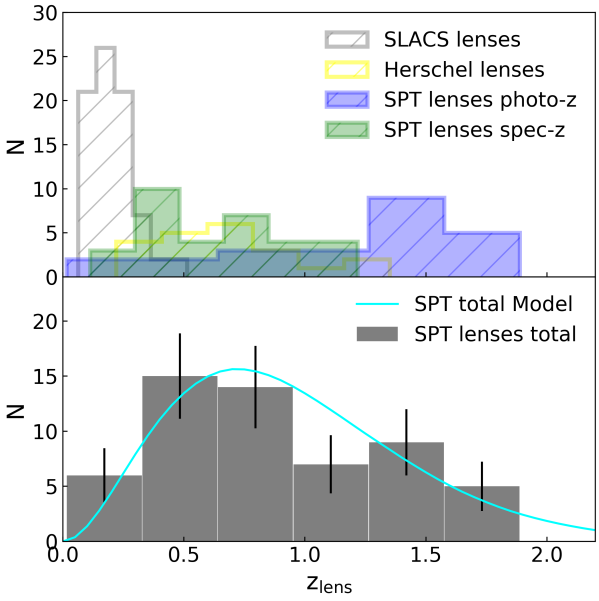

Figure 6. Model redshift distribution.

APPENDIX A: DESCRIPTIONS OF INDIVIDUAL LENSES FROM THE SPT SAMPLE

SPT0002-52 - This is a high-redshift lens ($z_{\rm lens} = 1.173$) while the corresponding SMG was found to have a redshift on the low end of the SPT-SMG distribution. ALMA imaging was conducted in band 3 and did not resolve the SMG into Einstein rings or even counter-images and so an Einstein radius and mass were not calculated for the lens. The lens was clearly detected in ISAAC's $K-$band, with poor detections in the shorter wavelengths. No IRAC imaging was conducted.

SPT0020-51 - This lens appears to be comprised of a group of three galaxies. Spilker et al. (2016), however, find the northern-most and brightest galaxy to have little effect on the lens model and hypothesize it to be at a different redshift than the remaining galaxies. The ALMA band 7 imaging resolves the SMG into a compact bright image and a faint counter-image centred on the south-west galaxy, suggesting the other galaxies detected in the near-IR are only influencing the lensing in a minor way. The south-west galaxy is undetected in the optical bands and IRAC fails to resolve the three galaxies. Furthermore SExtractor fails to resolve the three galaxies as well. The multi-band photometry therefore is a summation of all three galaxies.

SPT0027-50 - This lens is a complex group lens. Spilker et al. (2016) find the most reasonable model to contain three galaxies. SExtractor once again fails to resolve the three galaxies and the multi-band photometry therefore is a summation of all three galaxies. With the assumption that they all have the same redshift, a $K-z$ redshift was determined. ALMA band 7 imaging clearly resolves the SMG into two images.

SPT0103-45 - This lens consists of a bright central core and an arced feature to the south, visible most clearly in the SPIRE imaging. ALMA band 7 resolves the SMG into two images, seemingly unaffected by the southern arcs. Spilker et al. (2016) hypothesize the arcs of the lens to be either a tidal system or spiral arms. This lens is a candidate spiral lens.

SPT0106-64 - The physical extent of this lens, especially observed in the optical bands, is significantly larger compared to the other lenses in the sample. The same is not true in the near-IR. While the old stellar population therefore is fairly compact and central, the young stellar population spans a much larger halo. ALMA band 7 imaging resolves the SMG into two counter-images that reflect the physical size of the lens. Lens modeling for this system were not published by Spilker et al. (2016).

SPT0109-47 - This lens is a complex group lens, as indicated by a third counter-image of the SMG, imaged by ALMA band 7, that is further away from the central bright image than typical. Near-IR and optical imaging suggest the presence of two lensing galaxies, however, Spilker et al. (2016) required three in their lens model and were still not entirely able to reproduce the flux ratios between the three counter images. Photometry measurements were done on the north-east galaxy alone, while the spectroscopic redshift is for the south-west galaxy.

SPT0113-46 - This lens is modelled as a three galaxy system by Spilker et al. (2016). ALMA band 7 imaging resolves the SMG into a long arc with two counter images all centred on the bright, core galaxy of the lens with its companion lens galaxies located to the south-west and north-west of the central galaxy. SExtractor fails to resolve the three galaxies and the multi-band photometry therefore is a summation of all three galaxies, under the assumption that they all have the same redshift. A $K-z$ redshift was determined for the lens.

SPT0114-59 - While near-IR and optical imaging present a rather ordinary single galaxy lens, the ALMA band 7 resolved imaging depicts a central image with three counter images along a straight line to the south of the main image, suggesting a more complex lens. A $K-z$ redshift was determined for the lens and a photometric redshift is used for the SMG as well as no spectroscopic data was taken for this source. Consequently no lens modeling was conducted either.

SPT0125-47 - This lens is highly elongated along the south-east to north-west axis with a bright central bulge and is therefore likely a spiral galaxy viewed nearly perfectly edge-on. ALMA band 7 resolves the SMG into two images centred on the central bulge. Lens modeling done by Spilker et al. (2016) contains $\sim 6\sigma$ residuals which they discuss is likely due to an imperfect representation of the lens mass profile within their model.

SPT0125-50 - This lens is elongated along the north-east to south-west axis, however, no clear evidence of a disc-like feature is visible, so the lens is likely an elliptical galaxy with a high eccentricity. The two ALMA band 7 counter images are curved around the north-east corner of the lens indicating a large offset of the SMG from the optical line-of-sight axis.

SPT0147-64 - This lens is poorly detected across the optical and near-IR bands. The south-east component seen in $K-$band is used for photometry purposes. A $K-z$ redshifts was determined for this lens. ALMA imaging was done in band 3 and so the SMG was not resolved into individual components, consequently Spilker et al. (2016) did not conduct lens modeling.

SPT0150-59 - The physical extent of this lens is small, under $2''$ in diameter and the ALMA band 7 imaging resolves the SMG into a near perfect, compact Einstein ring. Lens modeling was not conducted for this lensing system. A $K-z$ redshifts was determined for this lens.

SPT0155-62 - This lens is only detected well in the $K-$band. It's physical extent is small, $\sim 1''$ in diameter. A $K-z$ redshifts was determined for this lens. ALMA band 7 imaging resolves the SMG once again into a near perfect, compact Einstein ring. Lens modeling was not conducted for this lensing system either.

SPT0202-61 - The primary lens, brightest in the $K-$band, appears to be loosely linked via a bridge to a secondary component to the south, which is not detected in the near-IR, however, is observed in the optical. A $K-z$ redshifts was determined for this lens. The Einstein rings of the SMG observed in ALMA's band 7 are centred on the northern component and do not appear to be affected by the southern one. Furthermore Spilker et al. (2016) make no mention of using a multi-component lens in their modeling. SExtractor cannot resolve the two components and so a summation of the two is used in multi-band photometry.

SPT0243-49 - This SMG is one of the highest redshift ($z_{\rm source} = 5.698$) sources of the SPT sample. It's high-resolution imaging is unable to resolve the source into multiple images even in ALMA's band 7. The lens contains an elongated, possibly tidal tail westward of the bright centre. A $K-z$ redshifts was determined for this lens.

SPT0245-63 - This lens is highly elongated along the south-east to north-west axis. No clear evidence of a disc-like feature is visible, so the lens is likely an elliptical galaxy with a high eccentricity. A $K-z$ redshifts was determined for this lens. ALMA's band 7 is unable to resolve the SMG into multiple imaging. Spilker et al. (2016) hypothesize that the ALMA imaging is of a massive foreground object, possibly

the lens itself, as lens modeling results in a lens mass much too small given the brightness of the lens in the near-IR. The SMG is one of the highest redshift sources in the SPT sample at $z_{\rm source} = 5.626$.

SPT0300-46 - This lens is poorly detected in the $K-$band, however, it is quite evident in the optical. A $K-z$ redshifts was determined for this lens. While ALMA's band 7 does not resolve the SMG into multiple images, Spilker et al. (2016)'s modeling find a two source model best represents the system, which is born out by the two velocity components found in the CO(4-3) line by (**?**).

SPT0311-58 - This SMG is the highest redshift ($z_{\rm source} = 6.9$) source of the SPT sample. The ALMA band 7 imaging resolves into a bright, main component and a faint counter image centred on the lens visible only in the near- and mid-IR. A $K-z$ redshifts was determined for this lens.

SPT0319-47 - This lens is best detected in the mid-IR, with poor-to-no detection in most of the optical bands. A $K-z$ redshifts was determined for this lens. ALMA band 7 is unable resolve the SMG into counter-images.

SPT0345-47 - This lens is best modelled by Spilker et al. (2016) by a single galaxy. In the near-IR SPIRE images slight extensions to the south-east and north-west can be seen possibly indicating the edge-on view of a spiral galaxy. This is hard to confirm visually because of the faintness of the lens in the other near-IR and optical imaging. A $K-z$ redshifts was determined for this lens.

SPT0346-52 - This SMG is one of the highest redshift ($z_{\rm source} = 5.656$) sources of the SPT sample. It's high-resolution imaging in ALMA's band 7 resolves the source into three components of similar flux, centred on a single galaxy as the lens. The results found by Spilker et al. (2016) largely confirm those found previously by (**?**). A $K-z$ redshifts was determined for this lens.

SPT0403-58 - This lens is identified as a blue lens as it's optical flux is significantly brighter than its near-IR flux. A $K-z$ redshifts was determined for this lens. Spectroscopic data was not taken for this SMG either, so a photometric redshift is used. ALMA band 7 does not resolve the SMG. Spilker et al. (2016) only find faint magnifications factors for the source.

SPT0404-59 - The single lens is detected in both optical and near-IR imaging. ALMA's band 7 resolves this SMG into two counter-images that are curved around the north-east corner of the lens indicating a large offset of the SMG from the optical line-of-sight axis. Spectroscopic analysis was not performed on the SMG and so a photometric redshift is used.

SPT0418-47 - The physical extent of the lens is one of the largest for a single galaxy lens in this sample and is detected robustly across all optical, mid- and near-IR bands. ALMA band 7 data shows the SMG to be a near perfect Einstein ring. Spilker et al. (2016) find this source to be one of the highest magnified SMGs of the SPT sample ($\mu_{870\,\mu{\rm m}} = 32$), an increase in magnification factor from that found by (**?**) which only had lower-resolution imaging of the source available to them.

SPT0441-46 - This lensing system is modelled by Spilker et al. (2016) by a single galaxy lens and a single component source, as is born out by optical and near-IR imaging of the lens, and the ALMA band 7 data which does not resolve the source into multiple images.

SPT0452-50 - This lens has the highest spectroscopic redshift of the SPT sample. Spilker et al. (2016) find only the southern object, visible in the optical, to be mildly lensing the SMG observed in ALMA band 7. The northern object seen in the optical imaging does not contribute to the lensing.

SPT0459-58 - This lens is only robustly detected in the mid-IR. A $K-z$ redshifts was determined for this lens using a lower limit $K-$band magnitude. This suggests the lens redshift is higher than the one used in this work.

SPT0459-59 - This lens is robustly detected across all bands observations were conducted in. Spilker et al. (2016) found there to be two components of the source being lensed with different magnification factors, one strongly lensed component and one fainter, barely lensed component.

SPT0512-59 - This lens is exceptionally bright across all optical, near-, and mid-IR bands. ALMA band 7 imaging resolves the SMG into well defined Einstein arcs with a large radius. Unfortunately a lens model has not yet been conducted for this lensing system.

SPT0516-59 - ALMA band 7 imaging suggests the southern, fainter object of the two observed in optical and near-IR imaging is the lens. Lens modeling, thus far not conducted, could confirm this. A $K-z$ redshift is determined for this lens.

SPT0529-54 - This lens is bright across all optical, near-, and mid-IR bands. The lens is slightly elongated along the east-west axis with a companion galaxy visible in the near-IR due west of the lens. Photometry measurements exclude the companion galaxy. Spectroscopic analysis shows this lens to be the lowest redshift lens of the SPT sample. ALMA band 7 high-resolution imaging resolves the SMG into a near-perfect Einstein ring centred on the main lens. Spilker et al. (2016) find large discrepancies with their model compared to (**?**) but found the differences to be accounted for completely by their use of ellipticity in the background source whereas (**?**) used circular symmetry.

SPT0532-50 - This lens is most clearly detected in the near-IR. ALMA band 7 imaging does not resolve the SMG into multiple images. Spilker et al. (2016) found a strong magnification factor of 10.

SPT0538-50 - This lens was observed across all optical, near- and mid-IR bands and is robustly detected in all. ALMA band 7 resolves the SMG into a near-perfect Einstein ring. Spilker et al. (2016) confirmed the need for two source-components in their modeling. They attributed this to the two velocity components found in CO(1-0) and CO(3-2) observations of the source. This lensing system was also discussed by (**?**) and (**?**).

SPT0544-40 - ALMA band 7 imaging shows a near-perfect Einstein ring with a sub-arcsec radius, implying a very low mass lens. Lens modeling has not yet been performed. A $K-z$ redshift was determined for this lens.

SPT0551-48 - This single galaxy lens results in a near-perfect Einstein ring imaging of the SMG with a sub-arcsec radius observed in ALMA band 7. Lens modeling has not yet been performed. A $K-z$ redshift was determined for this lens.

SPT0552-42 - The high-resolution ALMA band 7 imaging is a unique, asymmetric Einstein ring, centred on the western, fainter galaxy observed in the optical and near-IR. Due to the asymmetry of the SMG image, it is likely that the brighter galaxy to the east of the main lens is also contributing to the lensing. This can be confirmed by lens modeling, which has not yet been done. Photometry measurements were performed on the western lens. A $K-z$ redshift was determined for the lens.

SPT0555-62 - This lens is highly elongated along the south-east to north-west axis. In the optical a central bulge with fainter wings is visible. It is therefore likely a spiral galaxy viewed edge-on. A $K-z$ redshift was determined for this lens. ALMA band 7 resolves the SMG into three counter images centred on the central bulge of the lensing galaxy. Lens modeling has not yet been done for this lensing system.

SPT0604-64 - This lens produces near-perfect Einstein rings in the ALMA band 7 imaging of the SMG. The Einstein radius is larger than the physical extent of the lens, unlike the majority of observations in the SPT sample. This suggests a larger dark matter halo compared to most lenses. While in the optical bands the lens appears to be a single galaxy with the ALMA counters centred on it, in the near-IR the lens appears to either be elongated or have a companion to the south-east. The symmetry of the ALMA contours would suggest this second object in the near-IR does not contribute significantly to the lensing, which could be confirmed through lens modeling not yet conducted. A $K-z$ redshift was determined for the combined objects as SExtractor could not resolve the two.

SPT0625-58 - ALMA band 7 images the SMG in a "U-"shape centred on the lens. A $K-z$ redshift was determined for this lens. Lens modeling has not yet been conducted for this lensing system.

SPT2008-58 - The ALMA band 3 imaging of the SMG shows two counter-images, however, they are not centred on a galaxy in the optical or near-IR. This lens is therefore likely comprised of a group of galaxies. Photometry presented in this work corresponds to the galaxy at the eastern tip of the southern image, the brightest object nearby. A $K-z$ redshift was determined for this lens. Neither spectroscopic data for a redshift determination of the SMG or lens modeling for the system has been done.

SPT2031-51 - This is a single galaxy lens, as determined via lens modeling performed by Spilker et al. (2016). ALMA band 7 shows the SMG image as a tight arc with a counter image. Spectroscopic analysis was not performed on the SMG and so a photometric redshift was determined.

SPT2048-55 - This lens is a single low mass galaxy as suggested from the ALMA band 7 imaging of the SMG which has a small, sub-arcsec Einstein radius and is centred on the lens. Lens modeling done by Spilker et al. (2016) confirms this. A $K-z$ redshift was determined for this lens.

SPT2101-60 - This lens is highly elongated and appears to have a central bulge with thinner wings, suggesting it is a spiral galaxy viewed edge-on. Only the southern object, not the two northerly potential companions, was used in photometry measurements. A $K-z$ redshift was determined for this lens. A lensing model has not yet been done for this system.

SPT2103-60 - This lens is comprised of a group of galaxies. Spilker et al. (2016) find three foregrounds galaxies to be doing the lensing. The bright, northern most lensing galaxy was centred on during spectroscopic measurements for a redshift determination. Subsequently it was also used for photometry measurements. ALMA band 7 shows a unique shape to the images of the SMG, a typical lensing arc with two counter images that extend in a tail like fashion north-west ward.

SPT2132-58 - This lens is a single galaxy lens. A $K-z$ redshift was determined for this lens. The ALMA band 7 imaging barely resolves the SMG, which appears slightly off-centre from the lens. Spilker et al. (2016) predict a faint counter image in their best fit lens model.

SPT2134-50 - This lens is a single galaxy lens. ALMA band 7 resolves the SMG into a tight arc with a counter image centred on the lens. Lens modeling of Spilker et al. (2016) find the SMG to have a large magnification factor at 21.

SPT2146-55 - This lens is only detected in the near- and mid-IR. In SPIRE imaging it appears to be elongated with a central bulge, possibly indicating a spiral galaxy viewed edge on. The faint detections in ISAAC and the poor resolution of IRAC cannot confirm this though. A high $K-z$ redshift was determined for this lens, as suggested by the lack of detection in the optical. The SMG in resolved into two similarly bright counter images by ALMA band 7 imaging and is modelled by Spilker et al. (2016) as a single galaxy lens.

SPT2147-50 - This lens is a single galaxy lens. The ALMA band 7 resolved imaging is slightly off-centre of the foreground lens. Spilker et al. (2016) find a simple single object lensing system to best fit the data.

SPT2307-50 - This lens is difficult to define. ALMA band 3 displays a central bright image of the SMG as well as a faint counter image. The lens may either be the bright object to the north-east of the ALMA contours, the much smaller object to the south-west, or a combination of the two, potentially successively instead of simultaneously. Lens modeling, which has not yet been performed, will verify which object is the lens. Here we present photometry for the south-west lensing candidate. A $K-z$ redshift was determined for this lens. The bright object to the north-east has been confirmed via spectroscopy to be at $z=0.1$, which is likely too low to be an effective primary lens.

SPT2311-54 - This is a single galaxy lens. ALMA band 7 only marginally resolves this SMG. Spilker et al. (2016) find their model to represent the data well.

SPT2319-55 - Lens modeling performed by Spilker et al. (2016) confirms this to be a single galaxy lens, the south-west object not contributing to the lensing. ALMA band 7 resolves the SMG into two counter images separated by $\sim 1''$.

SPT2335-53 - Spectroscopy identifies the galaxy south-west of the ALMA band 3 image to be at a redshift of 0.0375 and is therefore unlikely to be the lens of the SMG. The significantly fainter object primarily detected in IRAC imaging centred on the ALMA contours was considered the lens instead. Photometry measurements and a $K-z$ redshift were determined for this galaxy. A lensing model has not yet been conducted for this lensing system.

SPT2340-59 - The two similarly bright images observed in the ALMA band 7 imaging of the SMG are centred on a lens with large physical extent. Despite the standard double-imaging of the SMG, Spilker et al. (2016) discuss the possibility that the two images are in fact two unlensed SMGs and not a single lensed SMG. They model both scenarios. In this work we assume a single SMG is being lensed.

SPT2349-50 - This is a single galaxy lens with a possible tidal feature extending to the north. Spilker et al. (2016) resolve the ALMA band 7 imaging into two components. No spectroscopic data was taken for this SMG so a photometric redshift is used instead.

SPT2354-58 - This single galaxy lens is observed well throughout the bands observed in. ALMA band 7 only slightly resolves the SMG. Spilker et al. (2016) are able to model the system well. The SMG has the lowest redshift of the SPT sample.

SPT2357-51 - This is a single galaxy lens clearly visible in the near- and mid-IR, less robustly detected in the optical. A $K-z$ redshift was determined for the the lens. The presence of the foreground lens suggests a lensing system despite the ALMA band 7 not resolving the SMG at all, as discussed in Spilker et al. (2016) who model the system and find a low magnification factor of ~ 2.9.

Table 3: Multi-band photometry, $m_{\rm AB}$. No entry if ALMA contours for lens not available. No entry if neither $z_{\rm lens}$ or $z_{\rm source}$ are known.

ID	G	R	J	K_s	CH1	CH2
SPT0002-52	-	> 23.61	-	19.2 ± 0.03	-	-
SPT0020-51	23.8 ± 0.04	-	20.1 ± 0.1	19.2 ± 0.06	-	19.4 ± 0.2
SPT0027-50	-	> 23.70	21.5 ± 0.3	19.7 ± 0.07	-	18.6 ± 0.1
SPT0103-45	> 24.72	23.2 ± 0.06	21.6 ± 0.2	20.2 ± 0.06	18.6 ± 0.1	18.3 ± 0.1
SPT0106-64	-	-	18.8 ± 0.04	18.5 ± 0.03	-	-
SPT0109-47	> 25.96	23.1 ± 0.03	-	20 ± 0.05	-	-
SPT0113-46	> 24.52	22.7 ± 0.04	20 ± 0.09	19 ± 0.03	18.6 ± 0.1	18.7 ± 0.2
SPT0114-59	-	-	21.8 ± 0.1	21.1 ± 0.2	-	-
SPT0125-47	21.4 ± 0.003	19.9 ± 0.001	17.9 ± 0.01	17.3 ± 0.009	17.7 ± 0.1	17.6 ± 0.09
SPT0125-50	-	20.8 ± 0.006	18.7 ± 0.04	18 ± 0.02	18.4 ± 0.1	18.6 ± 0.1
SPT0147-64	-	-	20.5 ± 0.06	19.8 ± 0.06	-	-
SPT0150-59	-	-	21.3 ± 0.05	20.2 ± 0.06	-	-
SPT0155-62	-	-	> 22.76	22 ± 0.1	-	-
SPT0202-61	-	> 24.28	21.2 ± 0.1	20.4 ± 0.07	-	-
SPT0243-49	> 24.39	23.8 ± 0.05	> 21.74	21.1 ± 0.2	20.8 ± 0.4	20.7 ± 0.4
SPT0245-63	20.9 ± 0.003	19.8 ± 0.002	-	17.8 ± 0.01	-	-
SPT0300-46	> 25.04	> 22.38	-	> 18.36	-	-
SPT0311-58	-	-	-	22.3 ± 0.4	21.2 ± 0.005	21.4 ± 0.006
SPT0319-47	> 24.11	-	21 ± 0.2	20.5 ± 0.1	20.1 ± 0.3	19.9 ± 0.3
SPT0345-47	-	-	23.3 ± 0.6	23 ± 0.6	-	-
SPT0346-52	-	> 23.58	> 23.55	21.6 ± 0.3	20.8 ± 0.4	20.4 ± 0.3
SPT0403-58	23.4 ± 0.04	23 ± 0.03	-	21.5 ± 0.1	-	-
SPT0404-59	> 25.15	23.8 ± 0.04	-	20.9 ± 0.1	-	-
SPT0418-47	-	19.4 ± 0.003	17.7 ± 0.02	17.5 ± 0.02	18 ± 0.1	18.1 ± 0.1
SPT0441-46	> 24.48	22.4 ± 0.01	20 ± 0.07	19.1 ± 0.03	19.1 ± 0.2	19.6 ± 0.2
SPT0452-50	> 24.89	> 24.10	-	20.5 ± 0.1	-	-
SPT0459-58	-	23.7 ± 0.09	21.1 ± 0.2	> 19.82	20.7 ± 0.4	20.4 ± 0.3
SPT0459-59	-	22.7 ± 0.06	-	19.5 ± 0.04	19 ± 0.2	19.2 ± 0.2
SPT0512-59	-	-	20.1 ± 0.1	18.6 ± 0.03	-	17.7 ± 0.1
SPT0516-59	-	-	21.6 ± 0.07	20.5 ± 0.09	20 ± 0.3	20 ± 0.3
SPT0529-54	-	-	-	-	-	17 ± 0.07
SPT0532-50	-	-	22 ± 0.2	20.1 ± 0.04	20.1 ± 0.3	-
SPT0538-50	-	-	18 ± 0.01	17.3 ± 0.008	17.6 ± 0.1	17.5 ± 0.09
SPT0544-40	-	-	22 ± 0.08	20.8 ± 0.04	-	-
SPT0551-48	> 26.38	> 24.13	20.9 ± 0.04	19.3 ± 0.05	-	-
SPT0552-42	-	> 23.36	21.3 ± 0.09	> 19.11	-	-
SPT0555-62	-	-	18.7 ± 0.009	17.8 ± 0.009	-	-
SPT0604-64	-	19.4 ± 0.006	18.1 ± 0.008	17.5 ± 0.01	-	-
SPT0625-58	-	> 22.98	21.1 ± 0.06	20.1 ± 0.07	-	-
SPT2008-58	-	-	20.3 ± 0.02	20.4 ± 0.06	-	-
SPT2031-51	> 24.48	22.4 ± 0.01	20 ± 0.1	19 ± 0.03	18.6 ± 0.2	18.4 ± 0.1
SPT2048-55	> 26.02	> 24.52	-	20.9 ± 0.09	-	-
SPT2101-60	-	-	18.6 ± 0.01	17.9 ± 0.01	-	-
SPT2103-60	-	23.4 ± 0.03	20.3 ± 0.1	19.2 ± 0.04	19 ± 0.2	-
SPT2132-58	-	-	20.9 ± 0.1	20.4 ± 0.08	-	-
SPT2134-50	> 24.42	22.6 ± 0.03	19.8 ± 0.07	18.9 ± 0.03	18.7 ± 0.2	18.7 ± 0.1
SPT2146-55	> 25.05	> 24.94	21.9 ± 0.4	21 ± 0.1	19.8 ± 0.3	19.6 ± 0.2
SPT2147-50	> 25.02	22.4 ± 0.02	19.6 ± 0.1	18.9 ± 0.06	18.6 ± 0.1	18.7 ± 0.2
SPT2307-50	-	-	-	20.8 ± 0.2	20.6 ± 0.03	20.8 ± 0.04
SPT2311-54	-	-	-	-	20.1 ± 0.3	20 ± 0.3
SPT2319-55	-	-	20.9 ± 0.1	20 ± 0.07	20.4 ± 0.3	20.5 ± 0.3
SPT2335-53	> 25.59	> 24.34	-	21.9 ± 0.4	22.2 ± 0.05	22.2 ± 0.05
SPT2340-59	18.2 ± 0.001	17.4 ± 0.001	-	16.2 ± 0.009	16.1 ± 0.05	16.5 ± 0.05
SPT2349-50	22.8 ± 0.009	21.4 ± 0.006	19 ± 0.04	18.7 ± 0.03	19.4 ± 0.01	19.1 ± 0.01
SPT2354-58	-	18.8 ± 0.003	18.4 ± 0.02	18 ± 0.03	18.2 ± 0.1	17.8 ± 0.1
SPT2357-51	> 24.19	> 23.70	-	-	20 ± 0.3	19.6 ± 0.2

Table 4: Redshifts and calculated astrophysical properties. † $K-z$ redshifts.

ID	$z_{\rm lens}$	$z_{\rm source}$	$L_{i-{\rm rest}}$ [10^{10} L$_\odot$]	M_i^* [10^{10} M$_\odot$]	$R_{\rm E}$ [$''$]	$M_{\rm E}$ [10^{10} M$_\odot$]
SPT0002-52	1.173	2.3513	-	-	-	-
SPT0020-51	0.751	4.1228	5.19 ± 0.6	23.2 ± 3	0.614 ± 0.007	10.9 ± 0.2
SPT0027-50	0.946†	3.4436	2.42 ± 0.7	10.8 ± 3	0.638 ± 0.007	15.2 ± 0.3
SPT0103-45	0.74	3.0917	1.23 ± 0.3	5.49 ± 1	0.88 ± 0.003	23.9 ± 0.2
SPT0106-64	0.48	4.91	6.35 ± 0.04	28.4 ± 0.2	-	-
SPT0109-47	0.669	3.6137	-	-	1.3 ± 0.03	46 ± 2
SPT0113-46	0.721†	4.2328	5.08 ± 0.4	22.8 ± 2	1.16 ± 0.01	37.3 ± 0.6
SPT0114-59	1.372†	3.3p	5.74 ± 0.7	25.7 ± 3	-	-
SPT0125-47	0.305	2.5148	3.39 ± 0.009	15.2 ± 0.04	1.01 ± 0.002	14.5 ± 0.06
SPT0125-50	0.51	3.959	-	-	0.984 ± 0.005	20.5 ± 0.2
SPT0147-64	0.98†	4.8036	7.34 ± 0.4	32.8 ± 2	-	-
SPT0150-59	1.085†	2.7881	4.23 ± 0.2	18.9 ± 0.9	-	-
SPT0155-62	1.656†	4.349	3.69 ± 0.5	16.5 ± 2	-	-
SPT0202-61	1.166†	5.018	5.9 ± 0.7	26.4 ± 3	0.758 ± 0.005	22.7 ± 0.3
SPT0243-49	1.372†	5.698	< 6.29	< 28.2	0.327 ± 0.003	4.61 ± 0.08
SPT0245-63	0.354†	5.626	4.51 ± 0.02	20.2 ± 0.07	-	-
SPT0300-46	0.53†	3.5954	0.489 ± 0.03	2.19 ± 0.1	0.337 ± 0.008	2.52 ± 0.1
SPT0311-58	1.752†	6.9	3.47 ± 1	15.5 ± 5	-	-
SPT0319-47	1.178†	4.51	7.04 ± 1	31.5 ± 5	0.283 ± 0.009	3.3 ± 0.2
SPT0345-47	1.949†	4.2957	2.53 ± 1	11.3 ± 6	0.306 ± 0.002	6.46 ± 0.08
SPT0346-52	1.542†	5.656	4.72 ± 1	21.1 ± 6	0.979 ± 0.007	45.3 ± 0.6
SPT0403-58	1.496†	4.2p	4.78 ± 0.4	21.4 ± 2	0.533 ± 0.05	15 ± 3
SPT0404-59	1.1	4.8p	-	-	0.549 ± 0.03	11.5 ± 1
SPT0418-47	0.265	4.224	3.24 ± 0.01	14.5 ± 0.05	1.25 ± 0.003	18.6 ± 0.09
SPT0441-46	0.882	4.477	8.23 ± 0.5	36.9 ± 2	0.678 ± 0.006	14.9 ± 0.3
SPT0452-50	1.218	2.0104	-	-	0.82 ± 0.1	52.3 ± 17
SPT0459-58	0.98†	4.857	4.07 ± 0.9	18.2 ± 4	0.468 ± 0.01	7.6 ± 0.5
SPT0459-59	0.938	4.7993	-	-	0.627 ± 0.02	13.2 ± 0.8
SPT0512-59	0.572	2.2331	2.51 ± 0.2	11.2 ± 1	-	-
SPT0516-59	1.203†	3.4045	4.48 ± 0.3	20 ± 1	-	-
SPT0529-54	0.14	3.369	2.74 ± 0.003	12.3 ± 0.01	1.36 ± 0.008	12.5 ± 0.1
SPT0532-50	1.15	3.399	2.7 ± 0.6	12.1 ± 3	0.556 ± 0.003	14 ± 0.2
SPT0538-50	0.404	2.7855	6.44 ± 0.02	28.8 ± 0.08	1.73 ± 0.004	54.2 ± 0.3
SPT0544-40	1.283†	4.2692	3.72 ± 0.3	16.7 ± 1	-	-
SPT0551-48	0.832†	2.5833	3.25 ± 0.1	14.6 ± 0.5	-	-
SPT0552-42	0.761†	4.437	1.72 ± 0.1	7.68 ± 0.6	-	-
SPT0555-62	0.363†	4.815	-	-	-	-
SPT0604-64	0.277†	2.48	-	-	-	-
SPT0625-58	1.07†	2.726	4.8 ± 0.3	21.5 ± 1	-	-
SPT2008-58	1.159†	-	12.4 ± 0.3	55.4 ± 1	-	-
SPT2031-51	0.624	2.2p	3.15 ± 0.3	14.1 ± 1	0.534 ± 0.005	8.34 ± 0.2
SPT2048-55	1.329†	4.089	-	-	0.361 ± 0.006	6.23 ± 0.2
SPT2101-60	0.403†	3.153	1.66 ± 0.02	7.42 ± 0.08	-	-
SPT2103-60	0.76	4.435	4.29 ± 0.4	19.2 ± 2	0.455 ± 0.009	5.97 ± 0.2
SPT2132-58	1.159†	4.768	7.67 ± 0.7	34.3 ± 3	0.335 ± 0.006	4.48 ± 0.2
SPT2134-50	0.776	2.78	6.92 ± 0.4	31 ± 2	0.518 ± 0.002	8.98 ± 0.07
SPT2146-55	1.332†	4.567	4.61 ± 2	20.7 ± 7	0.858 ± 0.004	33.6 ± 0.3
SPT2147-50	0.845	3.7602	10.7 ± 1	48.1 ± 5	1.2 ± 0.006	46.9 ± 0.5
SPT2307-50	1.267†	3.105	-	-	-	-
SPT2311-54	0.44	4.2795	1.9 ± 0.02	8.5 ± 0.1	0.209 ± 0.007	0.807 ± 0.05
SPT2319-55	0.91	5.2929	3.85 ± 0.5	17.2 ± 2	0.43 ± 0.003	5.94 ± 0.08
SPT2335-53	1.616†	4.757	3.92 ± 1	17.6 ± 6	-	-
SPT2340-59	0.109	3.864	3.83 ± 0.004	17.1 ± 0.02	1.58 ± 0.02	13.3 ± 0.3
SPT2349-50	0.45	2.8p	2.2 ± 0.02	9.85 ± 0.1	0.244 ± 0.005	1.19 ± 0.05
SPT2354-58	0.428	1.867	4.03 ± 0.05	18 ± 0.2	0.321 ± 0.003	2.15 ± 0.04
SPT2357-51	-	3.0703	-	-	0.215 ± 0.003	-

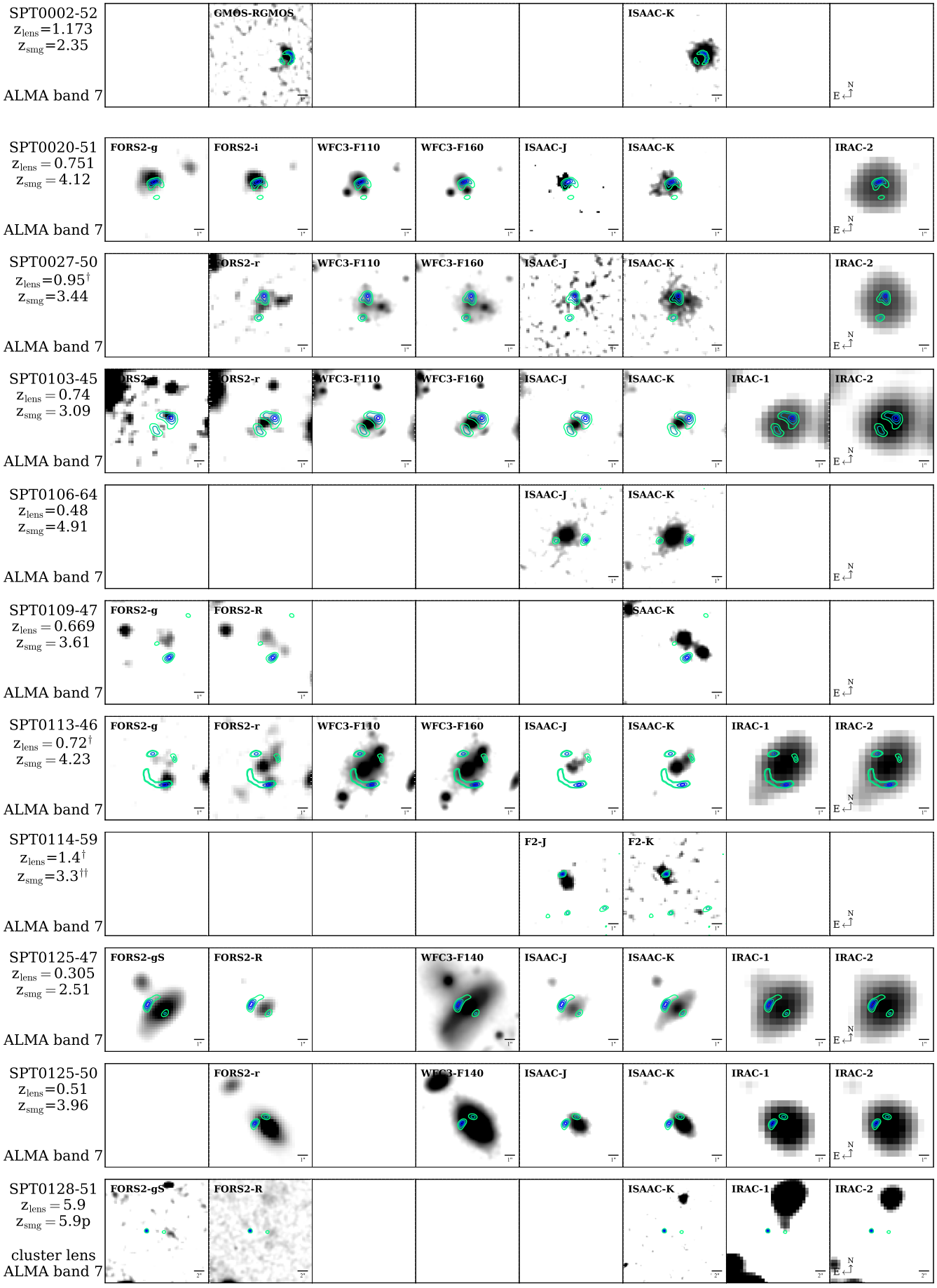
SPT0002-52
z_{lens}=1.173
z_{smg}=2.35
ALMA band 7
GMOS-RGMOS
ISAAC-K
SPT0020-51
z_{lens} = 0.751
z_{smg} = 4.12
ALMA band 7
FORS2-g
FORS2-i
WFC3-F110
WFC3-F160
ISAAC-J
ISAAC-K
IRAC-2
SPT0027-50
z_{lens}=0.95†
z_{smg}=3.44
ALMA band 7
FORS2-r
WFC3-F110
WFC3-F160
ISAAC-J
ISAAC-K
IRAC-2
SPT0103-45
z_{lens} = 0.74
z_{smg} = 3.09
ALMA band 7
FORS2-r
WFC3-F110
WFC3-F160
ISAAC-J
ISAAC-K
IRAC-1
IRAC-2
SPT0106-64
z_{lens}=0.48
z_{smg}=4.91
ALMA band 7
ISAAC-J
ISAAC-K
SPT0109-47
z_{lens} = 0.669
z_{smg} = 3.61
ALMA band 7
FORS2-g
FORS2-R
ISAAC-K
SPT0113-46
z_{lens} = 0.72†
z_{smg} = 4.23
ALMA band 7
FORS2-g
FORS2-r
WFC3-F110
WFC3-F160
ISAAC-J
ISAAC-K
IRAC-1
IRAC-2
SPT0114-59
z_{lens}=1.4†
z_{smg}=3.3††
ALMA band 7
F2-J
F2-K
SPT0125-47
z_{lens} = 0.305
z_{smg} = 2.51
ALMA band 7
FORS2-gS
FORS2-R
WFC3-F140
ISAAC-J
ISAAC-K
IRAC-1
IRAC-2
SPT0125-50
z_{lens}=0.51
z_{smg}=3.96
ALMA band 7
FORS2-r
WFC3-F140
ISAAC-J
ISAAC-K
IRAC-1
IRAC-2
SPT0128-51
z_{lens} = 5.9
z_{smg} = 5.9p
cluster lens
ALMA band 7
FORS2-gS
FORS2-R
ISAAC-K
IRAC-1
IRAC-2
N
E

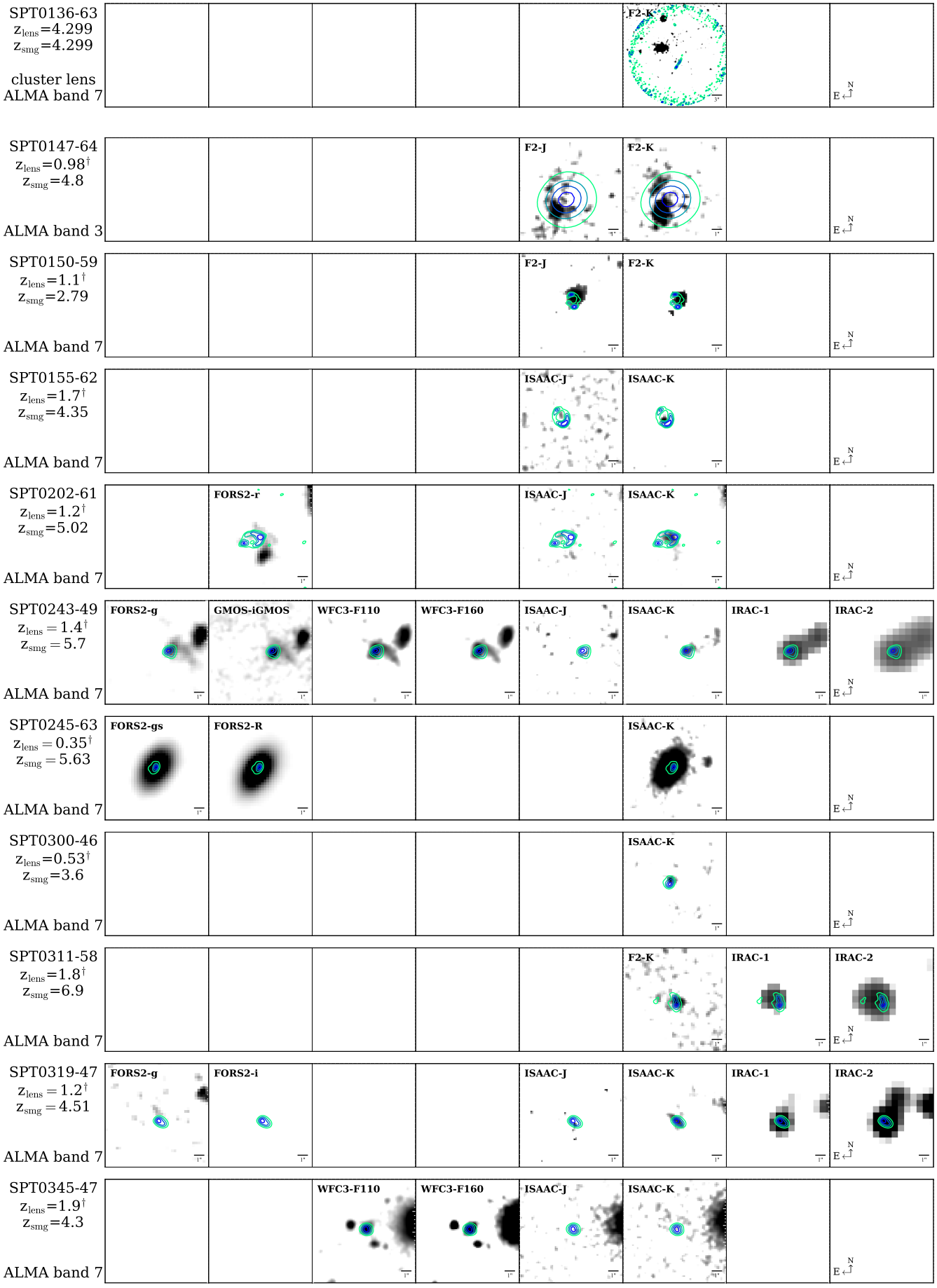
SPT0136-63
z_{lens}=4.299
z_{smg}=4.299
cluster lens
ALMA band 7
F2-K
SPT0147-64
z_{lens}=0.98†
z_{smg}=4.8
ALMA band 3
F2-J
F2-K
SPT0150-59
z_{lens}=1.1†
z_{smg}=2.79
ALMA band 7
F2-J
F2-K
SPT0155-62
z_{lens}=1.7†
z_{smg}=4.35
ALMA band 7
ISAAC-J
ISAAC-K
SPT0202-61
z_{lens}=1.2†
z_{smg}=5.02
ALMA band 7
FORS2-r
ISAAC-J
ISAAC-K
SPT0243-49
z_{lens} = 1.4†
z_{smg} = 5.7
ALMA band 7
FORS2-g
GMOS-iGMOS
WFC3-F110
WFC3-F160
ISAAC-J
ISAAC-K
IRAC-1
IRAC-2
SPT0245-63
z_{lens} = 0.35†
z_{smg} = 5.63
ALMA band 7
FORS2-gs
FORS2-R
ISAAC-K
SPT0300-46
z_{lens}=0.53†
z_{smg}=3.6
ALMA band 7
ISAAC-K
SPT0311-58
z_{lens}=1.8†
z_{smg}=6.9
ALMA band 7
F2-K
IRAC-1
IRAC-2
SPT0319-47
z_{lens} = 1.2†
z_{smg} = 4.51
ALMA band 7
FORS2-g
FORS2-i
ISAAC-J
ISAAC-K
IRAC-1
IRAC-2
SPT0345-47
z_{lens}=1.9†
z_{smg}=4.3
ALMA band 7
WFC3-F110
WFC3-F160
ISAAC-J
ISAAC-K
N
E

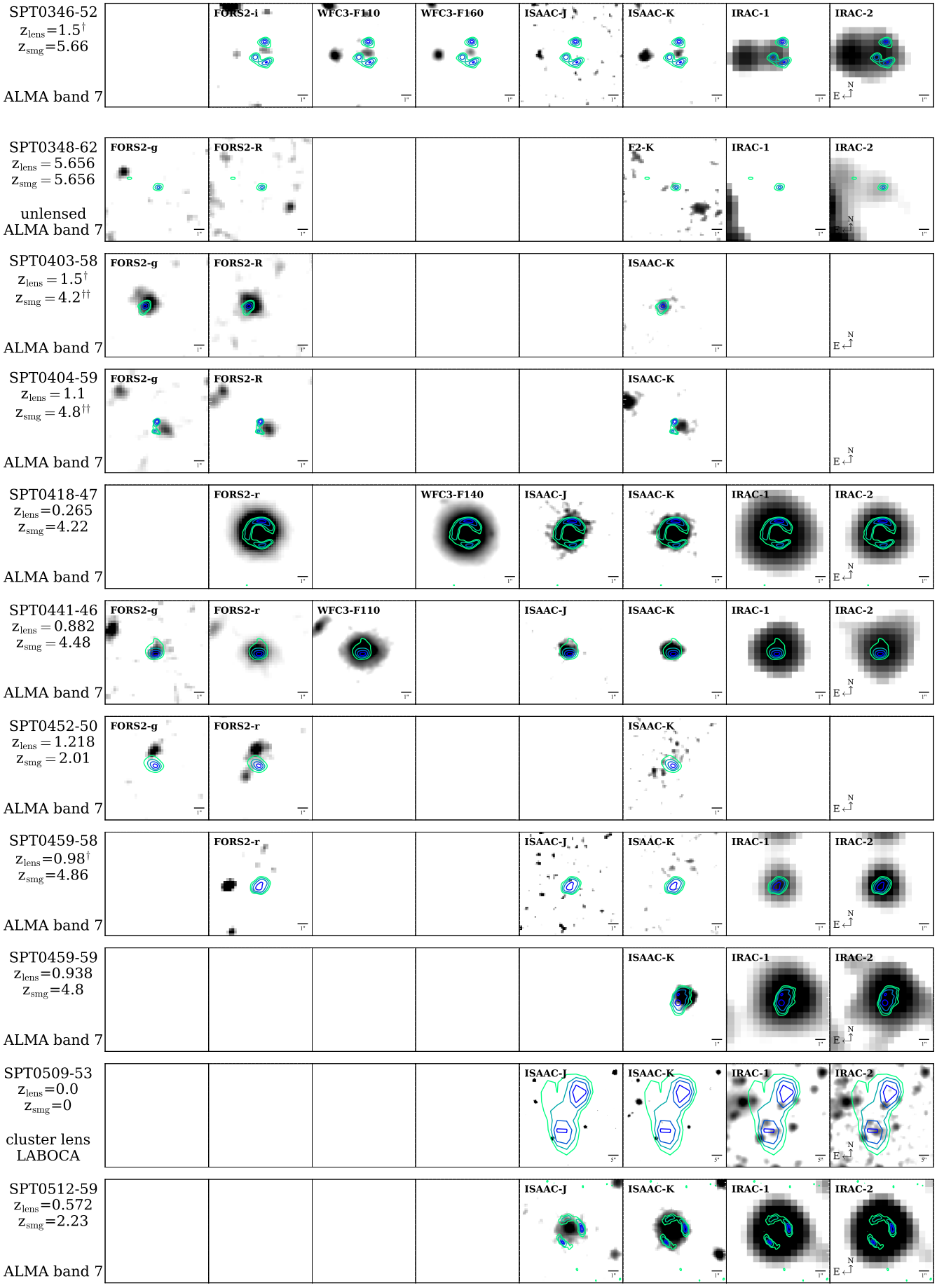
SPT0346-52
z_lens=1.5†
z_smg=5.66
ALMA band 7
FORS2-i
WFC3-F110
WFC3-F160
ISAAC-J
ISAAC-K
IRAC-1
IRAC-2
SPT0348-62
z_lens = 5.656
z_smg = 5.656
unlensed
ALMA band 7
FORS2-g
FORS2-R
F2-K
IRAC-1
IRAC-2
SPT0403-58
z_lens = 1.5†
z_smg = 4.2††
ALMA band 7
FORS2-g
FORS2-R
ISAAC-K
SPT0404-59
z_lens = 1.1
z_smg = 4.8††
ALMA band 7
FORS2-g
FORS2-R
ISAAC-K
SPT0418-47
z_lens=0.265
z_smg=4.22
ALMA band 7
FORS2-r
WFC3-F140
ISAAC-J
ISAAC-K
IRAC-1
IRAC-2
SPT0441-46
z_lens = 0.882
z_smg = 4.48
ALMA band 7
FORS2-g
FORS2-r
WFC3-F110
ISAAC-J
ISAAC-K
IRAC-1
IRAC-2
SPT0452-50
z_lens = 1.218
z_smg = 2.01
ALMA band 7
FORS2-g
FORS2-r
ISAAC-K
SPT0459-58
z_lens=0.98†
z_smg=4.86
ALMA band 7
FORS2-r
ISAAC-J
ISAAC-K
IRAC-1
IRAC-2
SPT0459-59
z_lens=0.938
z_smg=4.8
ALMA band 7
ISAAC-K
IRAC-1
IRAC-2
SPT0509-53
z_lens=0.0
z_smg=0
cluster lens
LABOCA
ISAAC-J
ISAAC-K
IRAC-1
IRAC-2
SPT0512-59
z_lens=0.572
z_smg=2.23
ALMA band 7
ISAAC-J
ISAAC-K
IRAC-1
IRAC-2

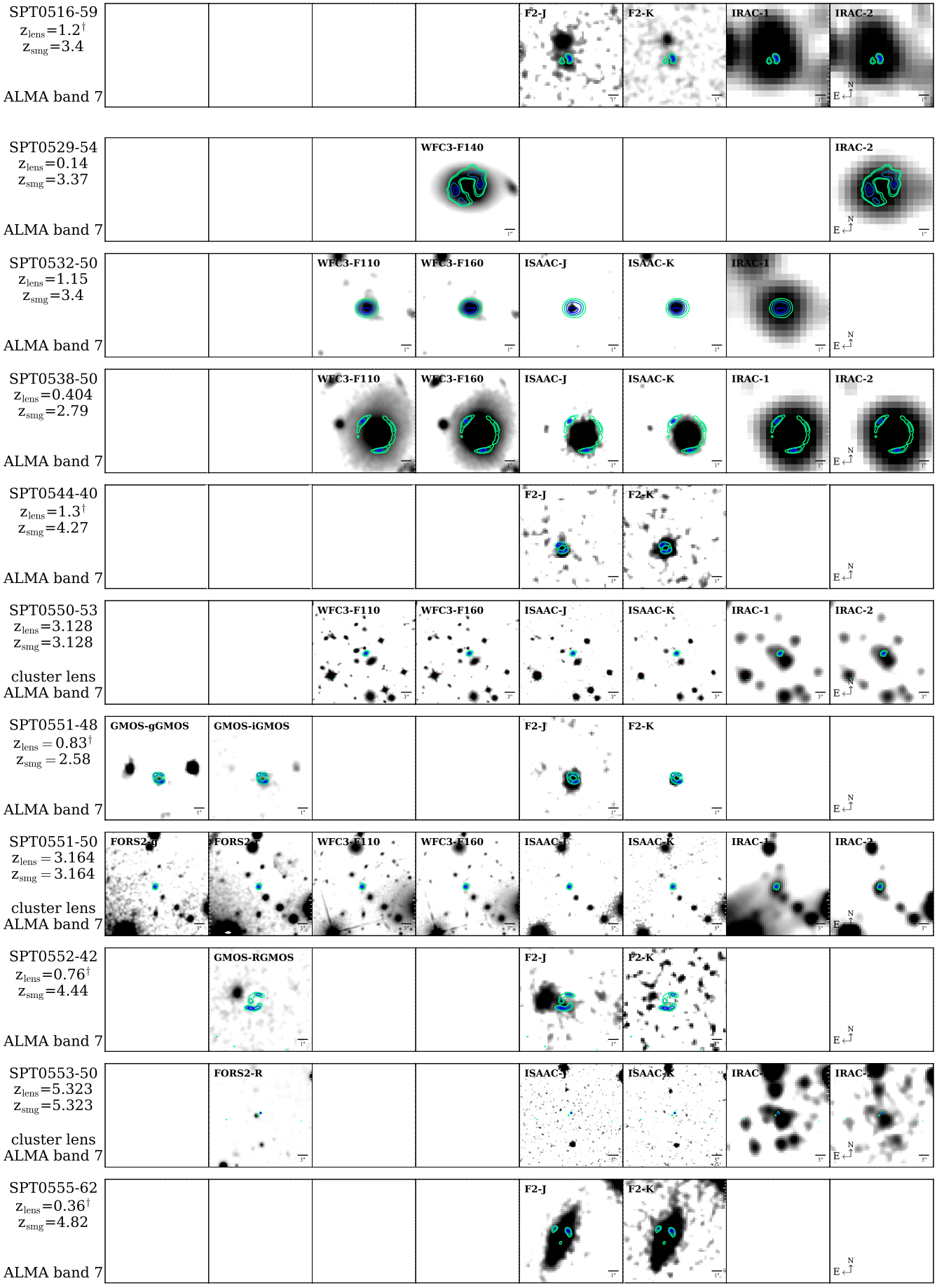
SPT0516-59
z_{lens}=1.2†
z_{smg}=3.4
ALMA band 7
F2-J
F2-K
IRAC-1
IRAC-2
SPT0529-54
z_{lens}=0.14
z_{smg}=3.37
ALMA band 7
WFC3-F140
IRAC-2
SPT0532-50
z_{lens}=1.15
z_{smg}=3.4
ALMA band 7
WFC3-F110
WFC3-F160
ISAAC-J
ISAAC-K
IRAC-1
SPT0538-50
z_{lens}=0.404
z_{smg}=2.79
ALMA band 7
WFC3-F110
WFC3-F160
ISAAC-J
ISAAC-K
IRAC-1
IRAC-2
SPT0544-40
z_{lens}=1.3†
z_{smg}=4.27
ALMA band 7
F2-J
F2-K
SPT0550-53
z_{lens}=3.128
z_{smg}=3.128
cluster lens
ALMA band 7
WFC3-F110
WFC3-F160
ISAAC-J
ISAAC-K
IRAC-1
IRAC-2
SPT0551-48
z_{lens} = 0.83†
z_{smg} = 2.58
ALMA band 7
GMOS-gGMOS
GMOS-iGMOS
F2-J
F2-K
SPT0551-50
z_{lens} = 3.164
z_{smg} = 3.164
cluster lens
ALMA band 7
WFC3-F110
WFC3-F160
SPT0552-42
z_{lens}=0.76†
z_{smg}=4.44
ALMA band 7
GMOS-RGMOS
F2-J
F2-K
SPT0553-50
z_{lens}=5.323
z_{smg}=5.323
cluster lens
ALMA band 7
FORS2-R
ISAAC-J
ISAAC-K
SPT0555-62
z_{lens}=0.36†
z_{smg}=4.82
ALMA band 7
F2-J
F2-K

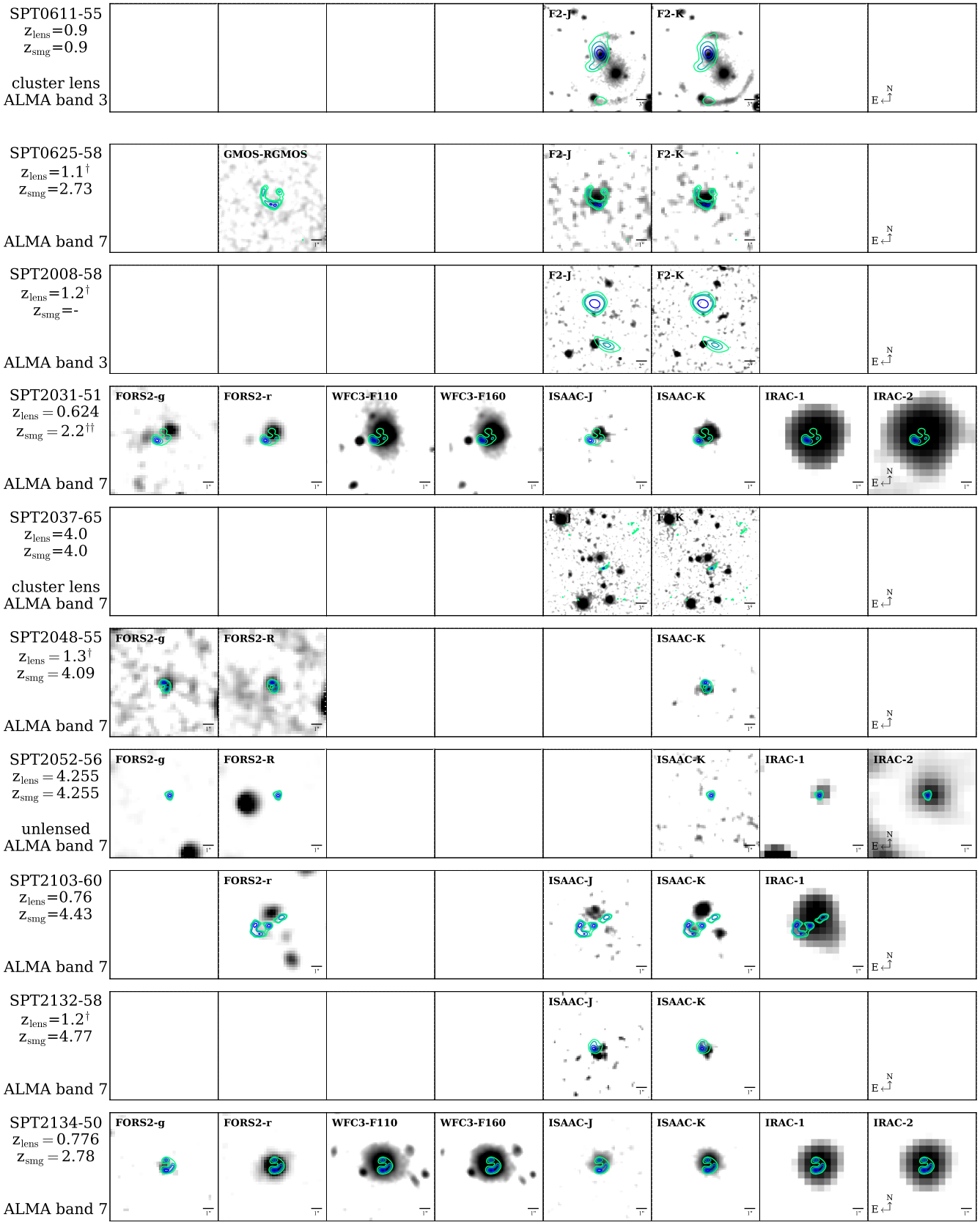
SPT0611-55
z_lens=0.9
z_smg=0.9
cluster lens
ALMA band 3
F2-J
F2-K
SPT0625-58
z_lens=1.1†
z_smg=2.73
ALMA band 7
GMOS-RGMOS
F2-J
F2-K
SPT2008-58
z_lens=1.2†
z_smg=-
ALMA band 3
F2-J
F2-K
SPT2031-51
z_lens = 0.624
z_smg = 2.2††
ALMA band 7
FORS2-g
FORS2-r
WFC3-F110
WFC3-F160
ISAAC-J
ISAAC-K
IRAC-1
IRAC-2
SPT2037-65
z_lens=4.0
z_smg=4.0
cluster lens
ALMA band 7
F2-J
F2-K
SPT2048-55
z_lens = 1.3†
z_smg = 4.09
ALMA band 7
FORS2-g
FORS2-R
ISAAC-K
SPT2052-56
z_lens = 4.255
z_smg = 4.255
unlensed
ALMA band 7
FORS2-g
FORS2-R
ISAAC-K
IRAC-1
IRAC-2
SPT2103-60
z_lens=0.76
z_smg=4.43
ALMA band 7
FORS2-r
ISAAC-J
ISAAC-K
IRAC-1
SPT2132-58
z_lens=1.2†
z_smg=4.77
ALMA band 7
ISAAC-J
ISAAC-K
SPT2134-50
z_lens = 0.776
z_smg = 2.78
ALMA band 7
FORS2-g
FORS2-r
WFC3-F110
WFC3-F160
ISAAC-J
ISAAC-K
IRAC-1
IRAC-2
N
E

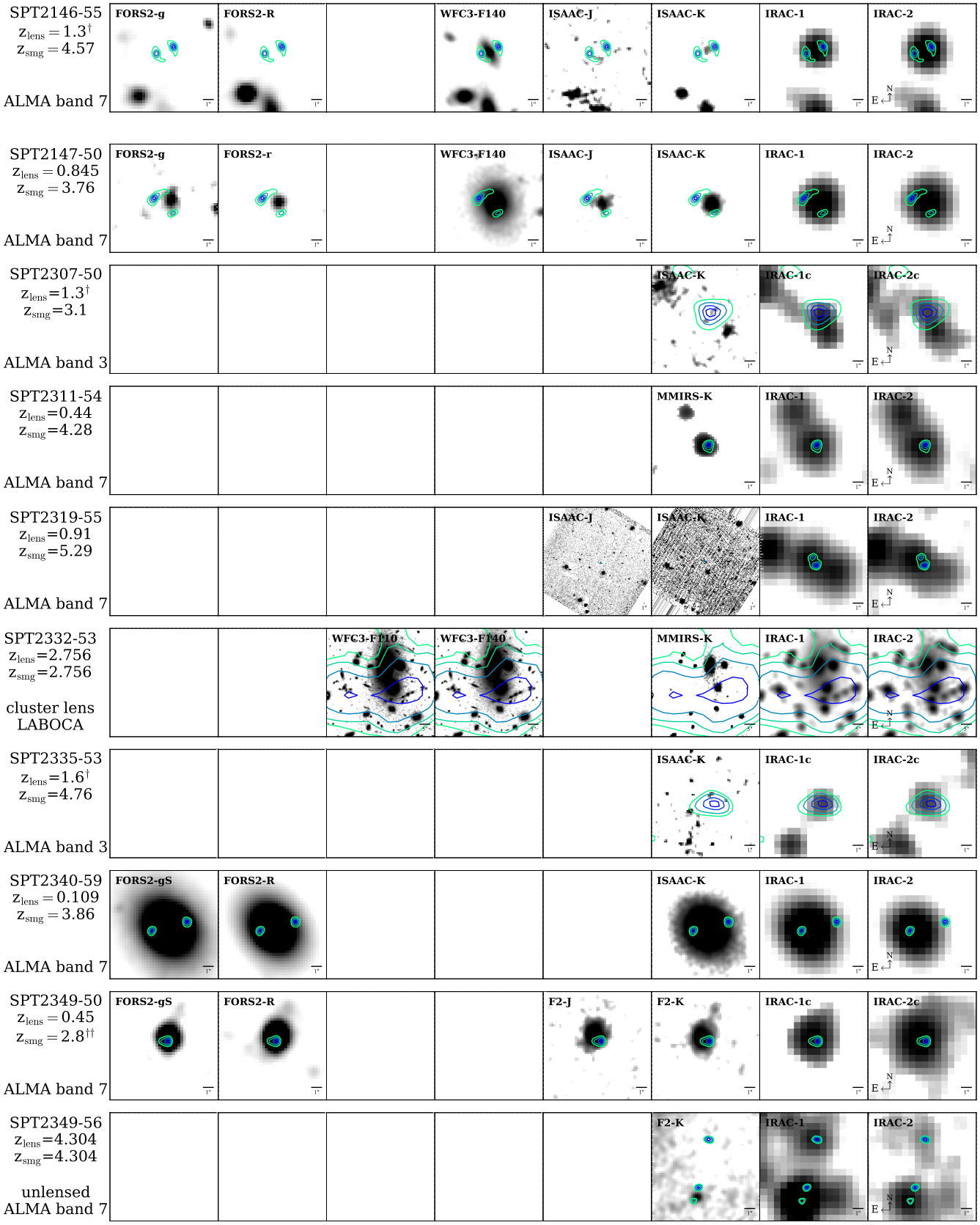
SPT2146-55
$z_{lens} = 1.3^{\dagger}$
$z_{smg} = 4.57$
ALMA band 7
FORS2-g
FORS2-R
WFC3-F140
ISAAC-J
ISAAC-K
IRAC-1
IRAC-2
SPT2147-50
$z_{lens} = 0.845$
$z_{smg} = 3.76$
ALMA band 7
FORS2-g
FORS2-r
WFC3-F140
ISAAC-J
ISAAC-K
IRAC-1
IRAC-2
SPT2307-50
z_{lens}=1.3†
z_{smg}=3.1
ALMA band 3
ISAAC-K
IRAC-1c
IRAC-2c
SPT2311-54
z_{lens}=0.44
z_{smg}=4.28
ALMA band 7
MMIRS-K
IRAC-1
IRAC-2
SPT2319-55
z_{lens}=0.91
z_{smg}=5.29
ALMA band 7
ISAAC-J
ISAAC-K
IRAC-1
IRAC-2
SPT2332-53
z_{lens}=2.756
z_{smg}=2.756
cluster lens
LABOCA
WFC3-F110
WFC3-F140
MMIRS-K
IRAC-1
IRAC-2
SPT2335-53
z_{lens}=1.6†
z_{smg}=4.76
ALMA band 3
ISAAC-K
IRAC-1c
IRAC-2c
SPT2340-59
$z_{lens} = 0.109$
$z_{smg} = 3.86$
ALMA band 7
FORS2-gS
FORS2-R
ISAAC-K
IRAC-1
IRAC-2
SPT2349-50
$z_{lens} = 0.45$
$z_{smg} = 2.8^{\dagger\dagger}$
ALMA band 7
FORS2-gS
FORS2-R
F2-J
F2-K
IRAC-1c
IRAC-2c
SPT2349-56
z_{lens}=4.304
z_{smg}=4.304
unlensed
ALMA band 7
F2-K
IRAC-1
IRAC-2
N
E

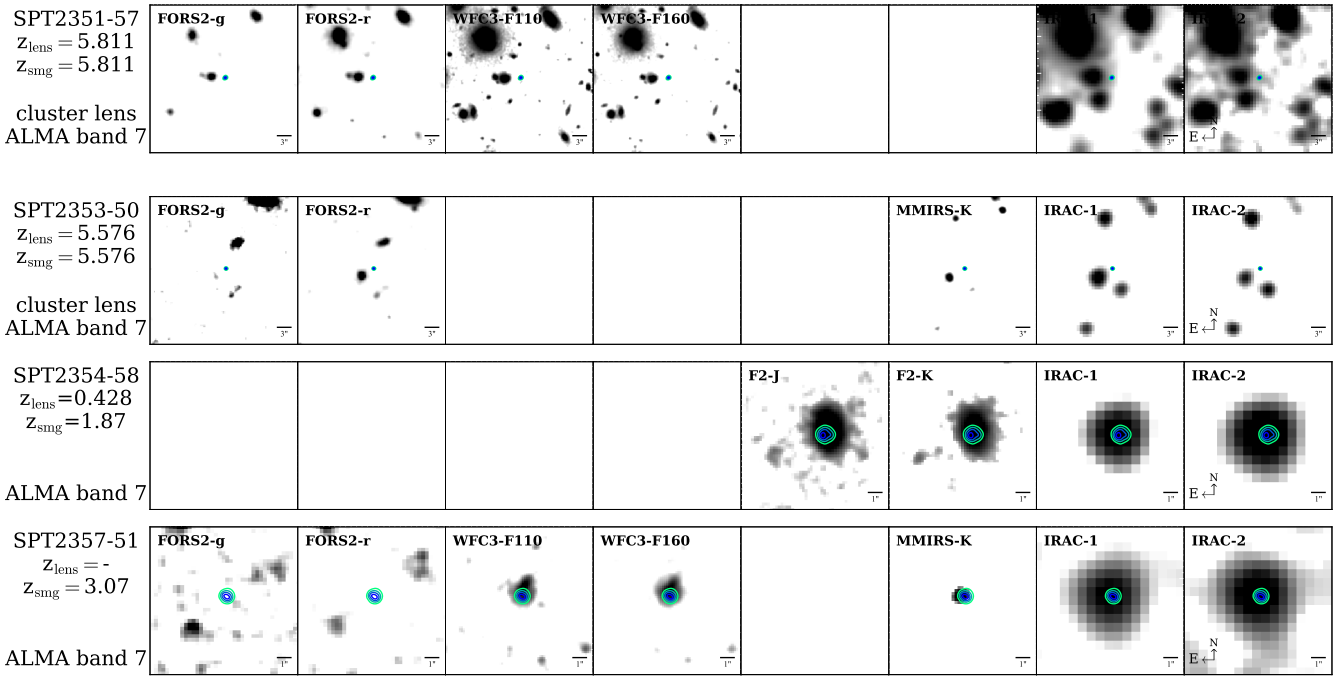
SPT2351-57
$z_{lens} = 5.811$
$z_{smg} = 5.811$
cluster lens
ALMA band 7
FORS2-g
FORS2-r
WFC3-F110
WFC3-F160
SPT2353-50
$z_{lens} = 5.576$
$z_{smg} = 5.576$
cluster lens
ALMA band 7
FORS2-g
FORS2-r
MMIRS-K
IRAC-1
IRAC-2
SPT2354-58
z_{lens}=0.428
z_{smg}=1.87
ALMA band 7
F2-J
F2-K
IRAC-1
IRAC-2
SPT2357-51
z_{lens} = -
z_{smg} = 3.07
ALMA band 7
FORS2-g
FORS2-r
WFC3-F110
WFC3-F160
MMIRS-K
IRAC-1
IRAC-2
N
E

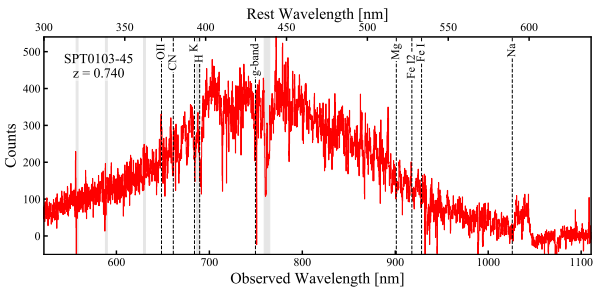
Rest Wavelength [nm]
SPT0103-45
z = 0.740
OII
CN
K
H
g-band
Mg
Fe
Fe
Fe
Na
Counts
Observed Wavelength [nm]

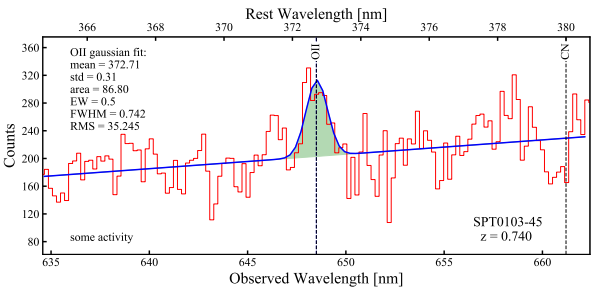
Rest Wavelength [nm]
OII gaussian fit:
mean = 372.71
std = 0.31
area = 86.80
EW = 0.5
FWHM = 0.742
RMS = 35.245
some activity
SPT0103-45
z = 0.740
OII
CN
Counts
Observed Wavelength [nm]

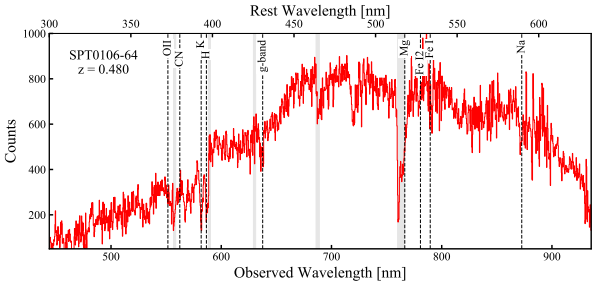
Rest Wavelength [nm]
SPT0106-64
z = 0.480
OII
CN
K
H
g-band
Mg
Fe
Fe
Fe
Na
Counts
Observed Wavelength [nm]

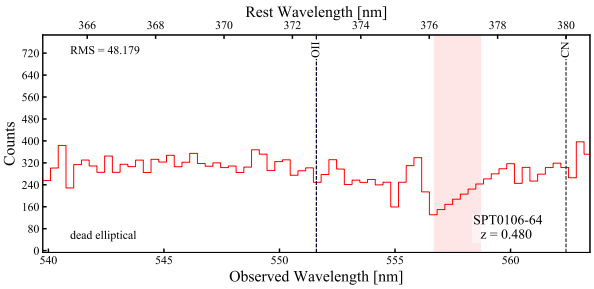
Rest Wavelength [nm]
RMS = 48.179
dead elliptical
SPT0106-64
z = 0.480
OII
CN
Counts
Observed Wavelength [nm]

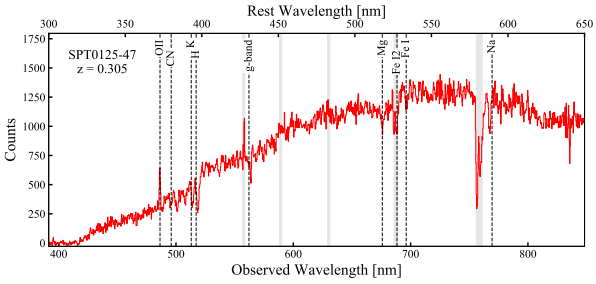
Rest Wavelength [nm]
SPT0125-47
z = 0.305
OII
CN
K
H
g-band
Mg
Fe
Fe
Na
Counts
Observed Wavelength [nm]

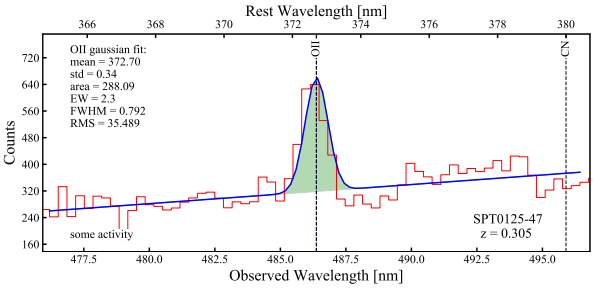
Rest Wavelength [nm]
OII gaussian fit:
mean = 372.70
std = 0.34
area = 288.09
EW = 2.3
FWHM = 0.792
RMS = 35.489
some activity
SPT0125-47
z = 0.305
OII
CN
Counts
Observed Wavelength [nm]

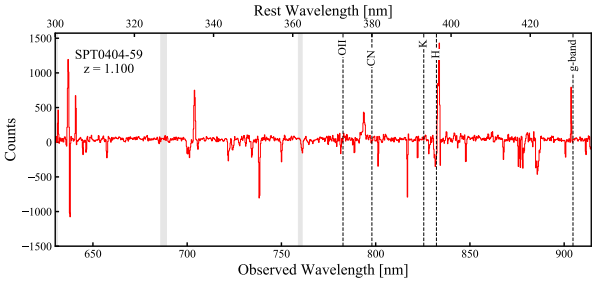
Rest Wavelength [nm]
SPT0404-59
z = 1.100
OII
CN
K
H
g-band
Counts
Observed Wavelength [nm]

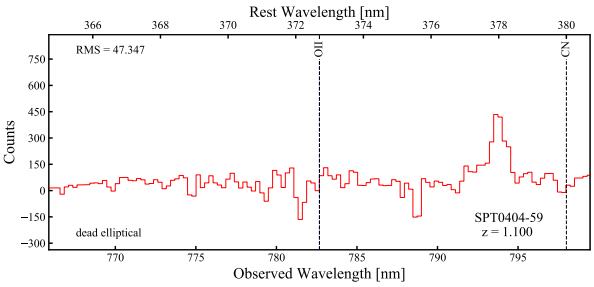
Rest Wavelength [nm]
RMS = 47.347
dead elliptical
SPT0404-59
z = 1.100
OII
CN
Counts
Observed Wavelength [nm]

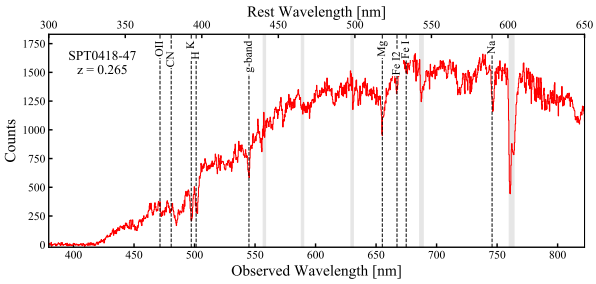
Rest Wavelength [nm]
SPT0418-47
z = 0.265
OII
CN
K
H
g-band
Mg
Fe
Fe
Na
Counts
Observed Wavelength [nm]

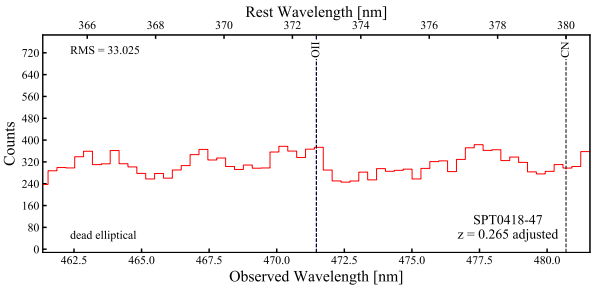
Rest Wavelength [nm]
RMS = 33.025
dead elliptical
SPT0418-47
z = 0.265 adjusted
OII
CN
Counts
Observed Wavelength [nm]

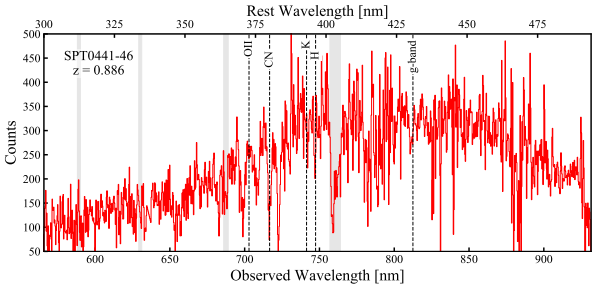
Rest Wavelength [nm]
SPT0441-46
z = 0.886
OII
CN
K
H
g-band
Counts
Observed Wavelength [nm]

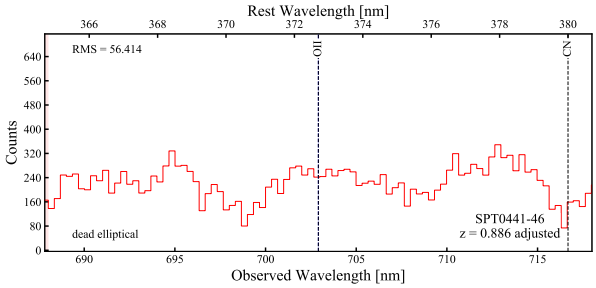
Rest Wavelength [nm]
RMS = 56.414
OII
CN
dead elliptical
SPT0441-46
z = 0.886 adjusted
Counts
Observed Wavelength [nm]

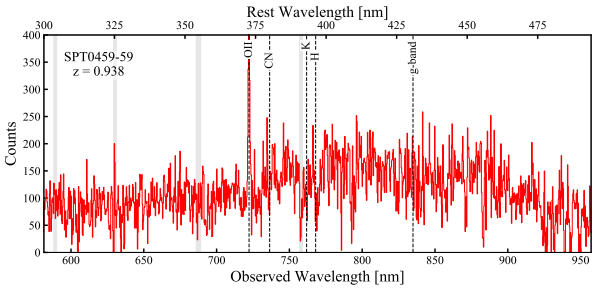
Rest Wavelength [nm]
SPT0459-59
z = 0.938
OII
CN
K
H
g-band
Counts
Observed Wavelength [nm]

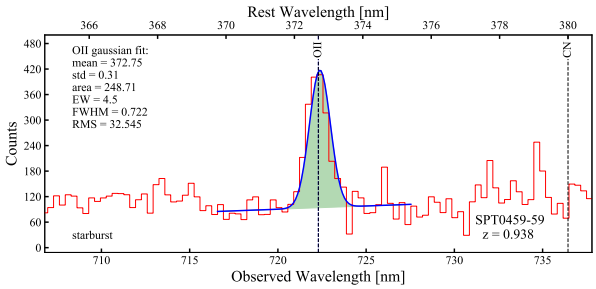
Rest Wavelength [nm]
OII gaussian fit:
mean = 372.75
std = 0.31
area = 248.71
EW = 4.5
FWHM = 0.722
RMS = 32.545
OII
CN
starburst
SPT0459-59
z = 0.938
Counts
Observed Wavelength [nm]

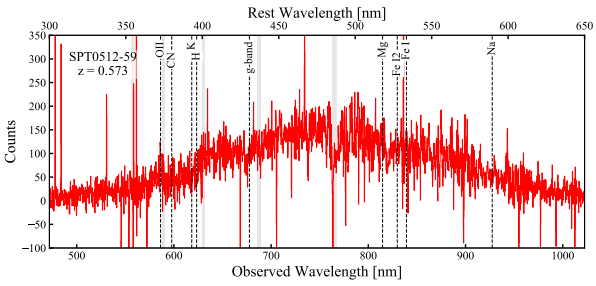
Rest Wavelength [nm]
SPT0512-59
z = 0.573
OII
CN
K
H
g-band
Mg
Fe I
Na
Counts
Observed Wavelength [nm]

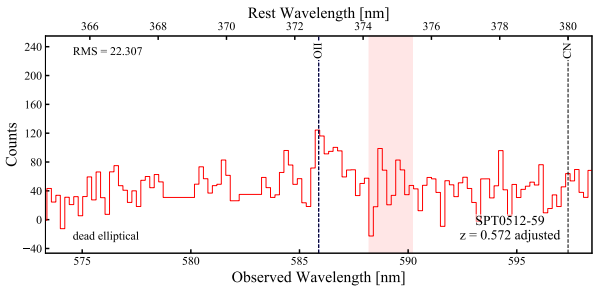
Rest Wavelength [nm]
RMS = 22.307
OII
CN
dead elliptical
SPT0512-59
z = 0.572 adjusted
Counts
Observed Wavelength [nm]

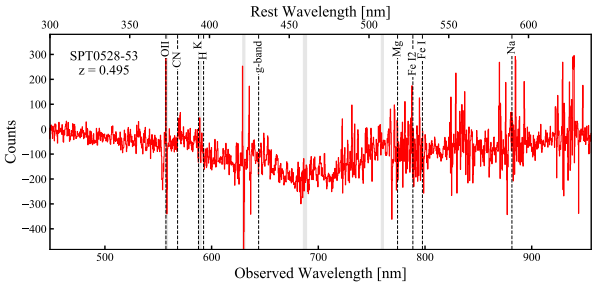
Rest Wavelength [nm]
SPT0528-53
z = 0.495
OII
CN
H
K
g-band
Mg
Fe I2
Fe I
Na
Counts
Observed Wavelength [nm]

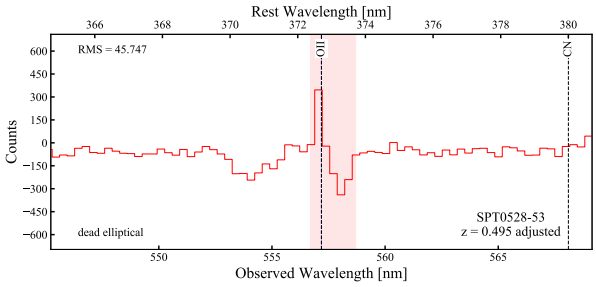
Rest Wavelength [nm]
RMS = 45.747
OII
CN
dead elliptical
SPT0528-53
z = 0.495 adjusted
Counts
Observed Wavelength [nm]

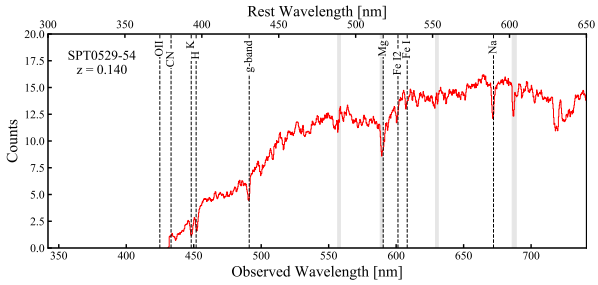
Rest Wavelength [nm]
SPT0529-54
z = 0.140
OII
CN
H
K
g-band
Mg
Fe I2
Fe I
Na
Counts
Observed Wavelength [nm]

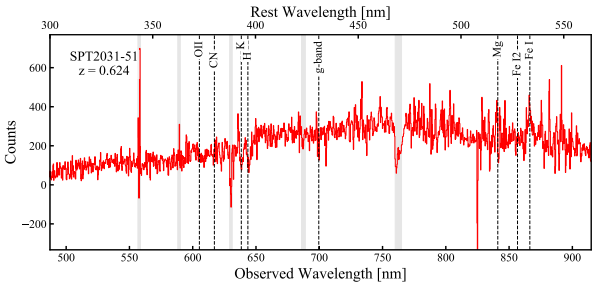
Rest Wavelength [nm]
SPT2031-51
z = 0.624
OII
CN
K
H
g-band
Mg
Fe I2
Fe I
Counts
Observed Wavelength [nm]

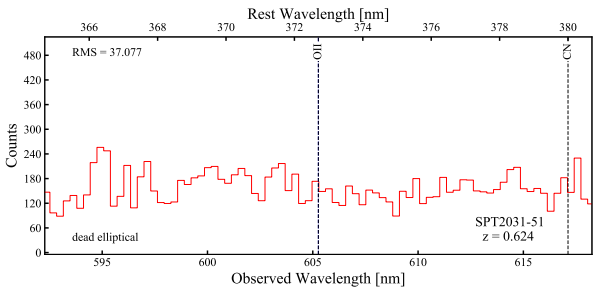
Rest Wavelength [nm]
RMS = 37.077
OII
CN
dead elliptical
SPT2031-51
z = 0.624
Counts
Observed Wavelength [nm]

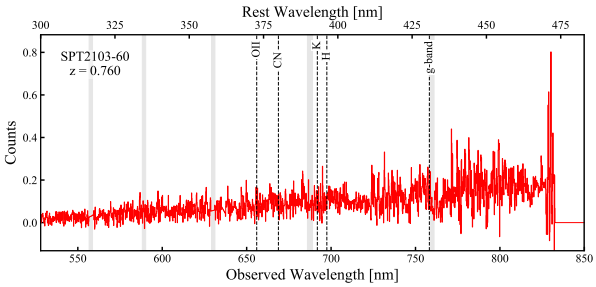
Rest Wavelength [nm]
SPT2103-60
z = 0.760
OII
CN
K
H
g-band
Counts
Observed Wavelength [nm]

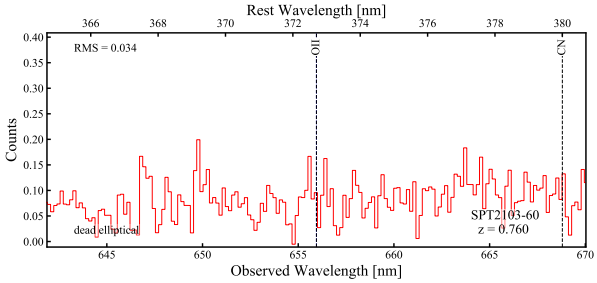
Rest Wavelength [nm]
RMS = 0.034
OII
CN
dead elliptical
SPT2103-60
z = 0.760
Counts
Observed Wavelength [nm]

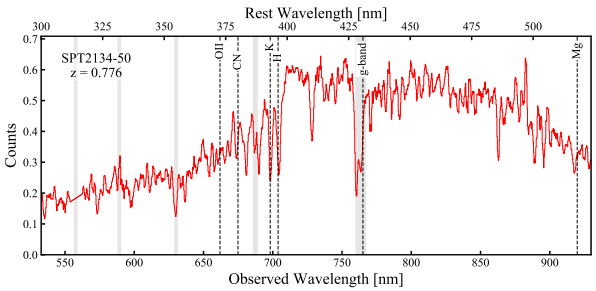
Rest Wavelength [nm]
SPT2134-50
z = 0.776
OII
CN
K
H
g-band
Mg
Counts
Observed Wavelength [nm]

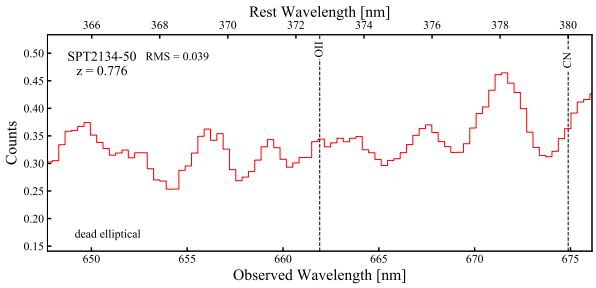
Rest Wavelength [nm]
SPT2134-50
z = 0.776
RMS = 0.039
OII
CN
dead elliptical
Counts
Observed Wavelength [nm]

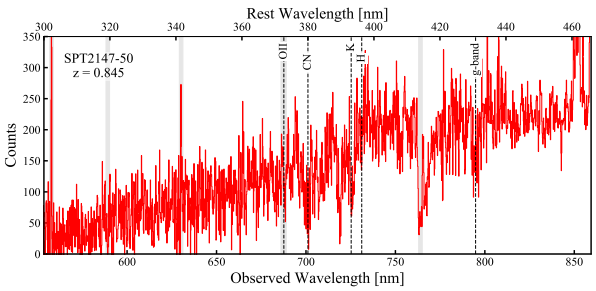
Rest Wavelength [nm]
SPT2147-50
z = 0.845
OII
CN
K
H
g-band
Counts
Observed Wavelength [nm]

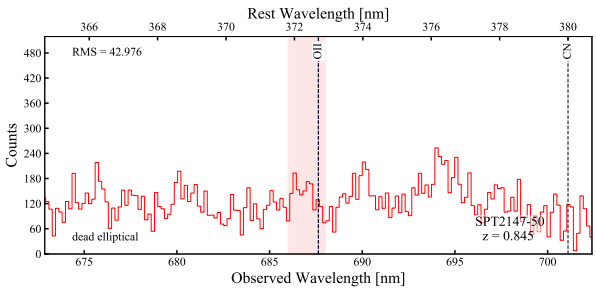
Rest Wavelength [nm]
RMS = 42.976
OII
CN
dead elliptical
SPT2147-50
z = 0.845
Counts
Observed Wavelength [nm]

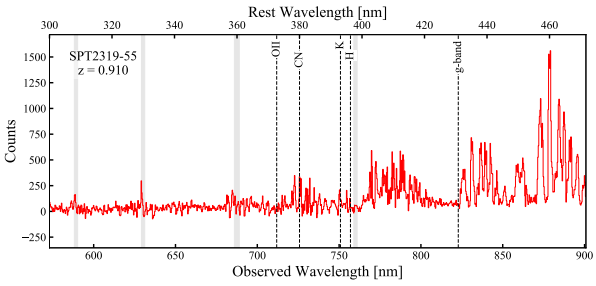
Rest Wavelength [nm]
SPT2319-55
z = 0.910
OII
CN
K
H
g-band
Counts
Observed Wavelength [nm]

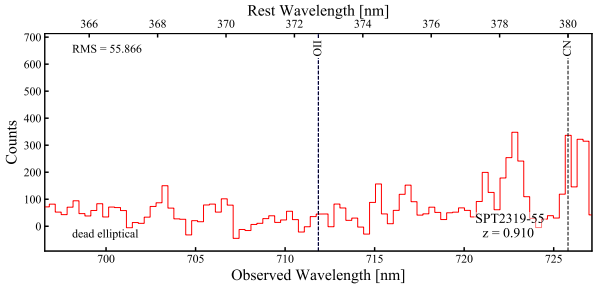
Rest Wavelength [nm]
RMS = 55.866
OII
CN
dead elliptical
SPT2319-55
z = 0.910
Counts
Observed Wavelength [nm]

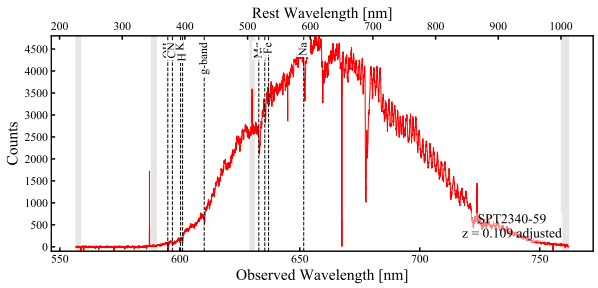
Rest Wavelength [nm]
Counts
CN
H
K
g-band
Mg
Fe
Na
SPT2340-59
z = 0.109 adjusted
Observed Wavelength [nm]

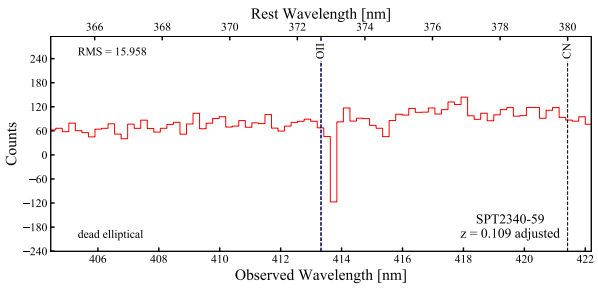
Rest Wavelength [nm]
RMS = 15.958
OII
CN
dead elliptical
SPT2340-59
z = 0.109 adjusted
Counts
Observed Wavelength [nm]

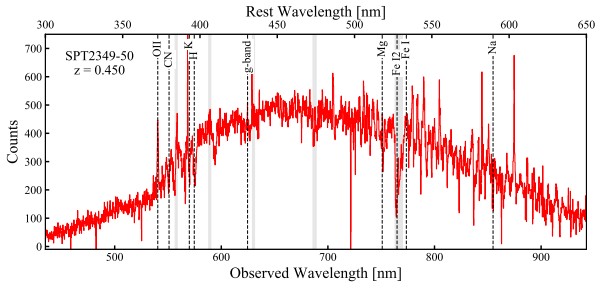
Rest Wavelength [nm]
SPT2349-50
z = 0.450
OII
CN
H
K
g-band
Mg
Fe I
Fe I
Na
Counts
Observed Wavelength [nm]

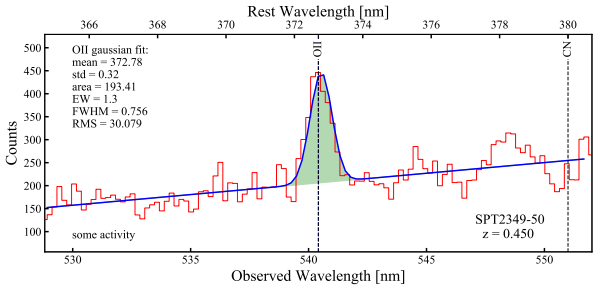
Rest Wavelength [nm]
OII gaussian fit:
mean = 372.78
std = 0.32
area = 193.41
EW = 1.3
FWHM = 0.756
RMS = 30.079
OII
CN
some activity
SPT2349-50
z = 0.450
Counts
Observed Wavelength [nm]

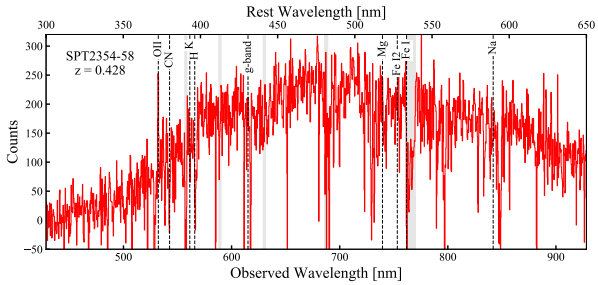
Rest Wavelength [nm]
SPT2354-58
z = 0.428
OII
CN
H
K
g-band
Mg
Fe I
Fe I
Na
Counts
Observed Wavelength [nm]

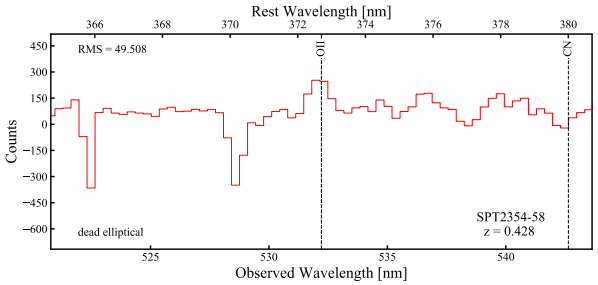
Rest Wavelength [nm]
RMS = 49.508
OII
CN
dead elliptical
SPT2354-58
z = 0.428
Counts
Observed Wavelength [nm]